Journal of Power Sources 624 (2024) 235511

Contents lists available at ScienceDirect

Journal of Power Sources

journal homepage: www.elsevier.com/locate/jpowsour

Pre-treated biomass waste melon peels for high energy density semi solid-state supercapacitors

Niyaz Ahmad [a,b], Alessia Rinaldi [a,b], Michele Sidoli [a,b], Giacomo Magnani [a,b,*], Vincenzo Vezzoni [a,b], Silvio Scaravonati [a,b], Lorenzo Pasetti [c], Laura Fornasini [c], Harsh Gupta [d], Michele Tamagnone [d], Francesca Ridi [e], Chiara Milanese [f], Mauro Riccò [a,b], Daniele Pontiroli [a,b]

[a] *Nanocarbon Laboratory, cIDEA & Department of Mathematical, Physical and Computer Sciences, University of Parma, Parco Area delle Scienze 7/A, 43124, Parma, Italy*
[b] *GISEL National Centre of Reference for Electrochemical Energy Storage Systems, INSTM National Interuniversity Consortium of Materials Science and Technology, Via Giusti 9, 50121, Firenze, Italy*
[c] *Department of Mathematical, Physical and Computer Sciences, University of Parma, Parco Area delle Scienze 7/A, 43124, Parma, Italy*
[d] *Istituto Italiano di Tecnologia, via Morego 30, 16163, Genova, Italy*
[e] *Department of Chemistry "Ugo Schiff" & C. S. G. I., University of Florence, Via della Lastruccia, 3, 50019, Sesto Fiorentino (FI), Italy*
[f] *Pavia Hydrogen Lab, Dipartimento di Chimica, Sezione di Chimica Fisica, Università di Pavia & C.S.G.I., Viale Taramelli 16, I-27100, Pavia, Italy*

HIGHLIGHTS

- Development of supercapacitors derived from melon peels waste.
- Highly performing ionic liquid-based gel polymer electrolytes.
- Optimized activation of biomass waste via chemical and physical processes.
- Up to 3.9 V stability window of gel polymer electrolyte.
- 31 Wh/kg specific energy and 860 W kg^{-1} power density.

GRAPHICAL ABSTRACT

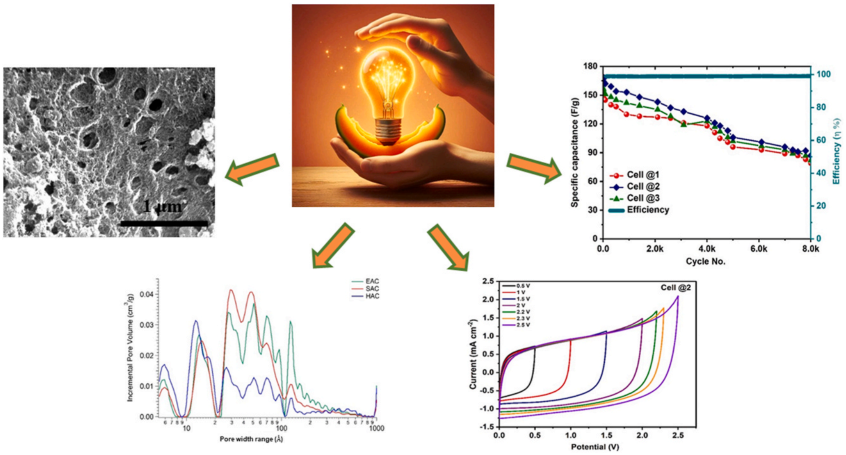

ARTICLE INFO

Keywords:
Gel polymer electrolyte
Ionic liquid
Supercapacitor

ABSTRACT

Semi-solid-state supercapacitors employing highly porous activated carbon (AC) electrodes are promising, cost-effective, and environmentally friendly energy storage devices with exceptional power performance. In this work, for the first time in literature, we report a comparative study on different pre-treatments made on melon waste starting precursor to produce hierarchical large surface area porous AC. Also, for the first time in our

---

* Corresponding author. Nanocarbon Laboratory, cIDEA & Department of Mathematical, Physical and Computer Sciences, University of Parma, Parco Area delle Scienze 7/A, 43124, Parma, Italy.

E-mail address: giacomo.magnani@unipr.it (G. Magnani).

https://doi.org/10.1016/j.jpowsour.2024.235511
Received 9 July 2024; Received in revised form 11 September 2024; Accepted 20 September 2024
Available online 27 September 2024

Biomass
Activated carbon

knowledge, a gel polymer electrolyte (GPE) consisting in lithium trifluoromethanesulfonate in ethylmethylimidazolium trifluoromethanesulfonate, with a high ionic conductivity (~3.3×10^{-3} S cm^{-1}) and a working voltage window of ~3.9 V vs Ag/Ag^{+}, was used. The supercapacitors were electrochemically characterized with electrochemical impedance spectroscopy, cyclic voltammetry, and galvanostatic charge-discharge tests. The working voltage window of the device was optimized in the range of 0–2.3V. Hydrothermally pre-treated AC-based supercapacitor is characterized by the best performance in terms of capacitance (~161–170 F g^{-1}), specific energy (29–31.34 Wh kg^{-1}), and power density (839–860 W kg^{-1}) at 1 A g^{-1}. Supercapacitors based on ACs pre-treated via hydrothermal and ethanol soaking outperform devices based on simple chemically/physically ACs in rate performance, while hydrothermally pre-treated AC demonstrates superior stability over 8000 cycles, exhibits initial 15 % capacitance fading and coulombic efficiency close to 99–100 %.

1. Introduction

Due to the globally increasing demand of versatile energy storage, devices such as supercapacitors and batteries have attracted significant attention in recent years [1,2]. In particular supercapacitors, with their high-power capabilities, are ideally suited for high-power pulse applications such as electric and hybrid vehicles, renewable energy systems, portable electronics, and industrial equipment [3,4]. Moreover, supercapacitors are characterized by wide operating temperature range performance, great cycling stability and low maintenance requirements [5]. These features make supercapacitors appealing for stationary and mobile applications, either as buffer systems in conjunction with batteries or as standalone energy storage devices. Charge storage in supercapacitors involves electric double-layer capacitance and pseudo-capacitance mechanisms to store and release energy [6]. Electric double-layer capacitance consists in the accumulation of electrolyte ions at the electrode-electrolyte interface, while pseudo-capacitance consists in reversible, unlocalized faradic charge-transfer reactions at the interface, which directly affect the energy density of the device [6].

In past years, different carbonaceous materials have been employed to increase energy efficiency in energy storage systems, from supercapacitors to metal-ion hybrid capacitors [7–9]. Activated carbons (ACs), carbon aerogels, carbon nanotube (CNTs), two-dimensional (2D) graphene, and carbon nanospheres, are some common supercapacitor electrode materials, due to their high ionic susceptible surface area and hierarchical porosity [7,10,11]. Because of the availability of precursor bio-waste materials, ACs are promising for manufacturing supercapacitor electrodes. Difficult-to-dispose wastes, derived from private dwellings, mass industry, animals, municipal rubbish, are ideal options for developing cost-effective and environmentally friendly electric double-layer capacitors (EDLCs) [12]. Different bio-wastes such as coconut shell, bamboo, coffee bean, banana peels, eggshell, poultry litter are reported in literature as potential materials to develop ACs for supercapacitor applications [12–17]. ACs can be produced through chemical activation, physical activation, or a combination of chemical and physical activation of waste biomass [18].

Cucumis melo L., also known as melon, is a member of the Cucurbitaceae family and one of the most widely cultivated fruits in tropical regions worldwide [19,20]. Its consumption is associated with both nutritional benefits and bioactive characteristics [19,20]. According to the Food and Agriculture Organization Corporate Statistical Database (2018), China is the largest producer of melon, with nearly 12.7 million tons per year, while its worldwide production is estimated to be 40 million tons per year [20]. Commercial processing of melon produces 8–20 million tons of waste (peels and seeds) per year worldwide which could be potential feedstock for producing ACs/biochar for electrochemical energy storage devices [21]. The chemical composition of melon peels is rich in lignin (26.46 %), hemicellulose (8.2 %), cellulose (27.68 %), ash and protein [20]. It has been estimated that, among all fruits and vegetables, melon is characterized by one of the highest waste ratios, with 55.3 % of the total weight being discarded [22]. For this reason, giving a second life to melon waste is paramount.

Across the literature, different pre-treatment methods to prepare ACs have been reported, such as physical, chemical, biological, and physicochemical activation processes, which are beneficial to obtain ACs with different kinds of surface area and porosity distributions [23–27]. As reported in this work, pre-treatment of carbon waste material with a hydrothermal process before activation appears as a promising step to prepare AC precursor. This approach proved to enrich carbon with oxygenated functional groups, improving the chemical activation of the precursor as compared to other pre-treatments [28]. Specifically, the hydrothermal treatment performed at moderate temperature (less than 350 °C) and pressure (less than 20 bars) induces reactions like hydrolysis of hemicellulose and dehydration, increasing the carbon fraction and improving the morphological properties of the final material [28]. Another possible pre-treatment route consists in soaking the raw biomass in an organic solvent, such as ethanol, methanol, butanol and tetrahydrofurfuryl alcohol, to remove lignin and hemicellulose from the lignocellulosic biowastes. This pre-treatment route significantly modifies the physical properties of ACs, in terms of specific surface area and porosity, and consequently can enhance, in combination with a proper electrolyte, the performance of the electrochemical devices [29–32].

To employ ACs in electrochemical energy storage devices, developing an optimized electrolyte is fundamental. In the latest years, gel polymer electrolytes (GPEs) have drawn significant attention for their application in supercapacitors, due to their notable properties, such as wide electrochemical working window, appropriate ionic conductivity (10^{-3} S cm^{-1}), broad thermal stability, and safety [2]. These features make GPEs a compelling alternative to traditional aqueous electrolytes, which suffer with low working voltage windows. Additionally, GPEs avoid the high flammability and volatility concerns associated with organic electrolytes, enhancing safety in operational environments [2]. Typically, GPEs consist in liquid electrolytes/ionic liquids (ILs)/salts dissolved in organic solvents, embedded in a host polymer matrix such as Poly(vinylidene fluoride-co-hexafluoropropylene) (PVdF-HFP), Polyethylene oxide, Polyvinyl alcohol, Poly(methyl methacrylate), Polyaniline, Poly(vinylidene fluoride) [33]. Typical electrolyte salts are characterized by large anions and low dissociation energy, to have easily dissociated and mobile ions, which act as charge carriers [34]. IL-based GPEs are characterized by superior electrochemical and thermal stability, non-flammability and non-volatility [35]. Various recent sources show that the addition of salts of Na/Li/Mg/Zn improves the electrochemical performance of GPEs, enhancing performances in supercapacitors [35–38].

In the present investigation, for the first time, a comparative analysis was conducted on supercapacitors designed with carbon electrodes derived from melon peels and featuring Li-ion based gel polymer electrolyte, to prove the feasibility of high-performance supercapacitors exploiting electrodes made from melon waste. To this end, raw melon peel powder was activated through a chemical/physical activation. To tune the physico-chemical properties of the resulting material, two pre-treatment methods were studied: powder was activated directly or after being pre-treated either through ethanol soaking (20–22 days) or through a hydrothermal process. The effects of the pre-treatments on highly porous carbon before activation were investigated with Brunauer–Emmett–Teller (BET) surface area and pore size analyses, X-ray diffraction (XRD), scanning electron microscopy (SEM) and Raman spectroscopy. The activated carbon electrodes, prepared via the aforementioned pre-treatments and activation, were employed in symmetrical semi solid-state EDLCs, featuring a novel Li-ion gel polymer electrolyte with superior performances. To study the electrochemical performances of the melon waste-derived materials and their interaction with the novel gel polymer electrolyte, the activated carbon electrodes were comparatively studied with electrochemical impedance spectroscopy (EIS), cyclic voltammetry (CV) and galvanostatic charge-discharge (GCD) measurements.

2. Experimental

2.1. Materials and device preparation

2.1.1. Preparation of ACs and carbon electrodes

Melon peels were removed with a knife during consumption of the fresh fruits kindly provided by a local Lombard organic farm (Pavia, Italy). The peels were freeze-dried and ground into powder using an electric grinder and then passed through a 500 μm sieve screen to obtain a homogeneous powder. Finally, to ensure proper preservation, the powders were stored in amber glass bottles at 4 °C until the use. The AC powders were prepared using three different procedures. For the first sample, called Simple Activated Carbon (SAC), melon powder was mixed with the activating agent $ZnCl_2$ ($\geq$99,8 % purity, Merck KGaA), in a 1:2 ratio in MilliQ water. The mixture was kept under constant stirring in a 60 °C bath for 12 h, and then was dried overnight in a 60 °C oven to obtain a well dispersed powder consisting of $ZnCl_2$-impregnated melon. Consequently, the activation stage was performed, which was maintained the same for each of the three experiments. This step was carried out by putting the powder mixture into an alumina boat and transferred in a tubular oven. After a vacuum and argon wash of the furnace, the sample was heated at a rate of 5 °C per minute up to around 800 °C, with a steady flow of argon gas. Once the temperature reached 800 °C, the argon gas supply was switched to CO_2-gas, and the furnace was kept at that temperature for 2 h to perform the physical activation. Subsequently, the resulting powder was washed with deionized (DI) water and 1 M HCl (fuming 37 %, Merck KGaA) solution to eliminate any remaining zinc and chloride ions and successively dried for 12 h at 90 °C before using it. The second method involved a hydrothermal pre-treatment to obtain Hydrothermal Activated Carbon (HAC). In this method, the melon waste powder was impregnated with the activating agent $ZnCl_2$ in 1:2 (wt:wt) ratio along with 20 ml of DI water. Then the powder was transferred into a Teflon lined autoclave vessel of 100 ml capacity and placed in a muffle at 330 °C for 12h [39], to perform a preliminary carbonization. After this treatment, the obtained powder ($ZnCl_2$-decorated hydro char) was thoroughly dried and then activated following the aforementioned activation treatment, described for the SAC sample, and subsequent washing. The third and last material, called Ethanol-soaked Activated Carbon (EAC), consisted in soaking the melon peels powder with ethanol (99,8 % purity, Merck KGaA) for about 20 days and then dried in an oven at ~ 90 °C for 24h. Then, the dried powder was used as a precursor for chemical and physical activation. The $ZnCl_2$ impregnation and the subsequent activation were carried out following the procedure described above for the SAC sample. The three syntheses are summarised in Fig. 1.

To produce supercapacitor electrodes, AC powders (80 % wt.) were mixed with carbon black (Timcal Super C 65, 10 wt%, 2 mg), a conductive additive, and PVdF-HFP (10 wt%, 2 mg, pellets, Merck KGaA), a polymeric binder. The mixture was mortared and dissolved in acetone (99 %, ACEF) to obtain thick slurries. Carbon black serves as an electron-transfer catalyst in addition to increasing the electrical conductivity of the electrode material [29], while the plastic binder is needed to keep the active material together and adherent to the current collector. The resulting slurries were then drop cast on circular flexible graphite sheets (16 mm diameter), pre-treated by vacuum drying for 12–16 h at a temperature of 90 °C.

2.1.2. Preparation and characterization of the GPE-film

To analyse the capacitive performance of the carbon powders, the GPE -film was prepared via “solution cast” method. 1 g of the host polymer PVdF-HFP was dissolved in 20 ml acetone, which was used as a solvent. A homogenous solution was obtained by stirring it constantly at room temperature for 10–14 h. Then, 4 g of 1 M lithium trifluoromethanesulfonate (LiTf, 99.995 % purity, Merck KGaA) in 1-ethyl-3-methylimidazolium trifluoromethanesulfonate (EMITf, $\geq$98.0 %, Merck KGaA) were added to the solution and stirred for another 10–14 h at room temperature. Subsequently, PVdF-HFP/1M LiTf in EMITf was transferred to a glass Petri dish, and acetone was allowed to slowly evaporate to produce a flexible GPE-film. After three to four days, a free-standing, flexible GPE was obtained. To prevent moisture absorption, the gel film has been retained in a dry atmosphere.

The GPE-film was electrochemically characterised by measuring the ionic conductivity and electrochemical stability window (ESW). EIS was used to test the ionic conductivity of the GPE-film throughout a fre-

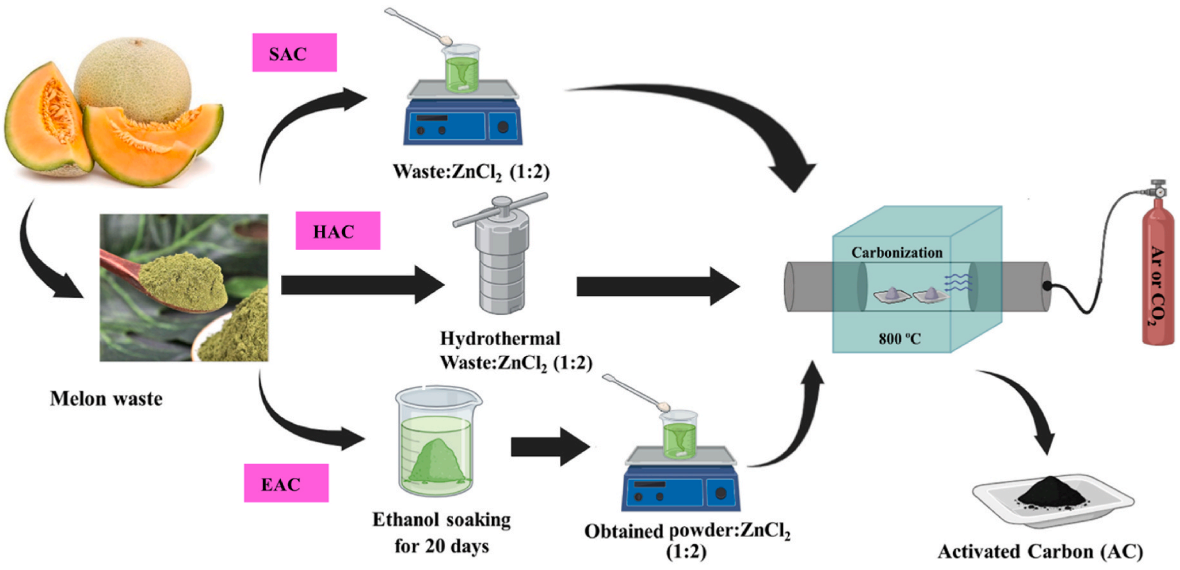

Fig. 1. Progressive preparation methods for Melon waste-based ACs with pre-treatment steps.

quency range of 10^5 Hz–0.1 Hz on a cell arrangement SS|GPE-film|SS, while ESW was evaluated using linear sweep voltammetry (LSV) on the cell configuration SS|GPE-film|Ag, where SS is a stainless steel disc and Ag is a silver foil, operating respectively as the working and counter/(pseudo) reference electrodes. The stability window against lithium of the GPE-film was measured on a cell configuration SS|GPE-film|Li, where lithium works as counter/(pseudo) reference electrode. The lithium-ion transference number (t_{Li}^{+}) of the GPE film was measured on a cell configuration Li|GPE-film|Li with a potentiostatic polarization (ΔV) of 10 mV to result in a steady-state current. The t_{Li}^{+} was calculated from the equation:

$$t_{Li^+} = \frac{I_s\ (\Delta V - R_0 I_0)}{I_0\ (\Delta V - R_s I_s)} \qquad (1)$$

where initial (I_0) and final (I_S) currents, as well as bulk resistances R_0 and R_S (i.e., before and after polarization, respectively), were obtained using DC polarization and AC impedance spectroscopy measurements, respectively [40].

2.1.3. Fabrication and analyses of supercapacitors

The produced ACs were electrochemically tested by constructing EDLC cells with GPE between two symmetric carbon electrodes. To avoid the short-circuit between the two symmetric electrodes, the GPE was trimmed circularly to a slightly larger size than the two symmetric electrodes. Then, the obtained carbon electrodes and GPE-films were sandwiched together in the AC | electrolyte | AC geometry. EDLC cells were designed in the following arrangement:

Cell @1: SAC | GPE-film | SAC

Cell @2: HAC | GPE-film | HAC

Cell @3: EAC | GPE-film | EAC

In the two electrode configurations, all the designed EDLCs were analyzed using EIS, CV, and GCD. EIS tests were performed using an alternate current with an amplitude of 10 mV and a frequency range of 10^5 Hz to 10 mHz. EIS and CV measurements were carried out using a 1010E Interface Potentiostat (Gamry Instruments, USA) electrochemical workstation, while GCD and cyclic investigations were carried out with a charge-discharge unit (Landt CT2001A, China).

2.2. Material characterization techniques

2.2.1. Structural and morphological characterization

Nitrogen adsorption-desorption analysis was conducted at a temperature of 77 K using a 3Flex analyser (Micromeritics, Norcross, GA, USA). Prior to the analysis, the samples were placed in a FlowPrep apparatus (Micromeritics, Norcross, GA, USA) and underwent a nitrogen flux pretreatment for 4 h at 120 °C. Subsequently, the samples were placed in the 3Flex chamber and degassed for 2 h at 120 °C under vacuum. The total specific surface area (SSA) was determined using the BET method after confirming compliance with the Rouquerol criteria. Additionally, the external SSA was assessed using the t-plot analysis, employing the Statistical Thickness Surface Area (STSA) carbon black equation. The pore size distribution was determined both analysing the desorption branch using the Barrett-Joyner-Halenda (BJH) method and the Non-Local Density Functional Theory (NLDFT) calculation, for which the model for carbon material with open slit geometry - NLDFT (SD3) - was utilized.

The structural properties of the ACs and the presence of contaminants were studied via powder X-ray diffraction (PXRD), which was conducted using a D8 Discover diffractometer (Bruker Corporation, MA, USA), operating in Debye-Scherrer geometry configuration. A copper anode (CuKα), coupled with a Göbel mirror and a 0.5 mm collimator, was used as the X-ray radiation source. 2D diffraction patterns were captured using a MX225 detector (Rayonix, IL, USA). Images obtained from the PXRD experiments were processed utilizing the FIT2D software, and subsequent analysis of the extracted powder patterns was performed using the GSAS-II suite. During data collection, all samples were securely sealed within glass capillaries of 0.7 diameter and rotated to ensure uniform exposure.

The structural characteristics of ACs were further explored through micro-Raman measurements, conducted using a Horiba Jobin Yvon LabRam system (HORIBA Scientific, Kyoto, Japan). This system featured a confocal micro-spectrometer with a focal length of 300 mm. An Olympus BX40 microscope (Olympus, Tokyo, Japan) was used to navigate through the sample, while a ULWD 50× objective lens served for laser beam focusing and scattered photons collection. The objective lens utilized a grating with 1800 grooves/mm and was integrated with a motorized XY stage and a Peltier-cooled silicon CCD. A double Nd:YAG laser emitting at 473.1 nm served as the excitation source for micro-Raman spectroscopy. Spectral data were recorded in the range of 100–3500 cm^{-1}, employing the silicon peak at 520.6 cm^{-1} and the emission lines of a gas lamp as references for calibration in the low and high-wavenumber spectral ranges, respectively. To avoid potential heat-induced effects on the carbon samples, density filters were applied to reduce the excitation power of the laser beam. During analysis, a standard protocol involving 4 consecutive measurements of 30-s durations each was followed. The resulting spectrum was derived from the averaged spectra acquired during these measurements.

The microstructural analysis was conducted using SEM with a Helios Nanolab 650 instrument (FEI Company, OR, USA). The microscope operated at an accelerating voltage of 10–20 kV, and morphological images were acquired using secondary electron detection mode with magnification ranging from 10,000x to 500,000x. Sample preparation for SEM analysis involved the placement of samples onto conductive carbon tape affixed to an aluminium stub. To enhance the visualization of microstructural features, a few select samples were scanned at tilted angles to provide a more comprehensive analysis.

2.2.2. Electrochemical characterization

LSV, EIS, and CV measurements were conducted using a 1010E Interface Potentiostat (Gamry Instruments, PA USA). The analyses were carried out on both the "as prepared" electrolyte and on the final assembled EDLCs devices. LSV measurements were performed in a two-electrode configuration at a constant scan rate of 10 mV s^{-1}. These electrochemical techniques were employed to evaluate the operational voltage window of the GPE. EIS measurements were carried out over a frequency range of 10 mHz to 10^5 Hz by applying an alternate current signal of 10 mV. CV tests were conducted on the final EDLCs. Initially, CV scans were performed over different voltage ranges from 0 to 2.5 V at a constant scan rate of 10 mV s^{-1}. Subsequently, the optimized voltage range was maintained constant while varying the scan rate from 10 to 300 mV s^{-1}. These electrochemical techniques provided valuable insights into the performance and characteristics of the EDLCs, contributing to the comprehensive assessment of their electrochemical properties.

GCD analysis was conducted to assess the capacity, efficiency, and capacity retention of the supercapacitors synthesized from melon waste via various synthesis routes and employing GPE. The measurements were performed using a Landt CT2001A and a Neware (China) BTS-4008 (5V50 mA) battery testing system. GCD measurements were conducted employing both constant current (chronopotentiometry) and constant voltage (chronoamperometry) modes.

To determine the optimal working voltage ranges, the EDLCs were subjected to charge and discharge cycles at different voltage levels ranging from 0 to 2.5 V, maintaining a constant current of 1 A g^{-1}. Subsequently, the EDLCs underwent charge-discharge cycles at various current densities under the optimized voltage conditions. Additionally, the EDLCs were subjected to 8000 charge-discharge cycles at a constant current density of 1 A g^{-1}. These experimental procedures enabled a comprehensive evaluation of the performance characteristics of the supercapacitors derived from melon waste, facilitating insights into their performance and durability over repeated charge-discharge cycles.

3. Results and discussion

3.1. Electrochemical properties of GPE

The obtained GPE-film, consisting of liquid electrolyte 1M LiTf in EMITf immobilized in PVdF-HFP, demonstrates superior mechanical and electrochemical stabilities, with an ionic conductivity of approximately 10^{-3} S cm^{-1} at ambient temperature. The GPE used in this work is a free-standing, flexible, semi-transparent thick film of thickness 250–350 μm, as demonstrated in Fig. 2 (A). Several mechanical forces, including multiple bending, twisting, and stretching, were applied to the prepared film, as shown in Fig. 2(B–D) [29,41]. Flexibility tests shows that the GPE-film can be used to develop highly flexible and bendable devices. The ionic conductivity of GPE-film, measured by performing EIS on a cell configuration SS|GPE|SS, where SS is stainless steel, is ~3.3 × 10^{-3} S cm^{-1} at room temperature (~26 °C) [42].

For the evaluation of the ESW of the prepared GPE-film, a LSV measurement was carried out on a cell configuration SS|GPE|Ag (discussed above) in a two-electrode system [42]. The LSV curve of the GPE-film is represented in Fig. 2 (E) from −2.2 V to 3.5 V versus Ag/Ag^{+} at a scan rate of 10 mVs^{-1} [29]. The GPE-film stability is evident up to −1.4 V and 2.5 V versus Ag/Ag^{+} in the cathodic and anodic range respectively, and an overall electrochemical stability window of ~3.9 V is observed, which strongly suggests that it can be employed to design high performance supercapacitors and high working voltage window electrochemical devices in general. The electrochemical stability window of the GPE-film against lithium has also been measured on a cell configuration SS|GPE|Li in a two-electrode cell at room temperature, as shown in Fig. S1 † [43]. It has been found that the GPE-film is stable up to 4 V against lithium which shows it can be employed for the further applications such as lithium-ion batteries and capacitors.

The lithium-ion transference number (t_{Li}^{+}) of the GPE was measured by combining alternating current (AC) and DC techniques. The Li|GPE|

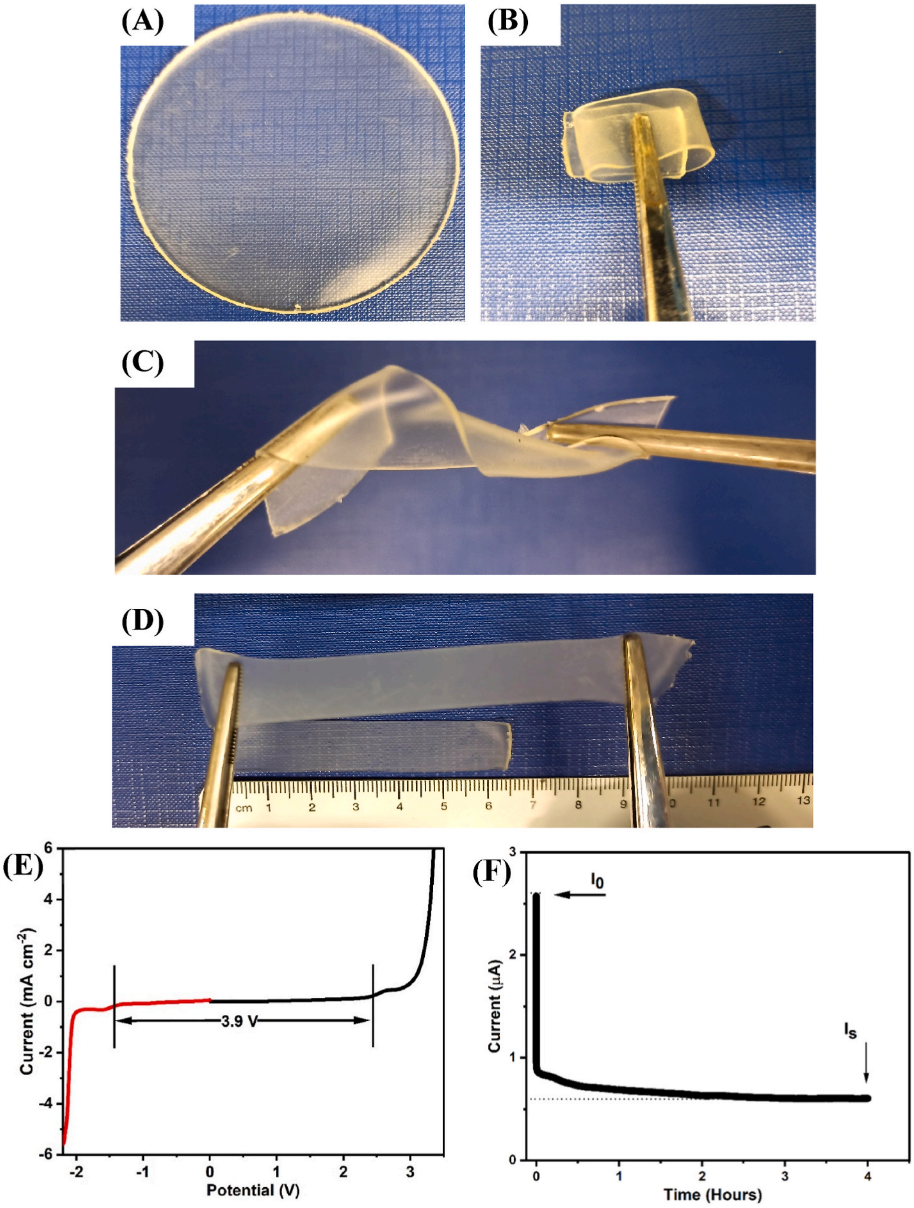

Fig. 2. (A–D) Images of GPE-film with some flexibility tests, in particular multiple bending, twisting, and stretching. (E) LSV measurement of GPE-film to evaluate its electrochemical stability window (F) dc polarization curve to evaluate the Li^{+} transference number of the GPE-film.

Li cell was polarized by a small signal of 10 mV for 4 h and the current variation as a function of time was obtained, as shown in Fig. 2 (F) [44]. Additionally, the EIS curves were also recorded on the same cell before and after DC polarization, as shown in Fig. S2 †. The $t_{Li}{}^{+}$ value was calculated by using equation (1) and found to be ~0.64. The obtained value of t_{Li}^{+} in the present GPE is found to be comparable or even better than several reported values of different GPEs across literature, which shows the suitability and diverse applicability of the present GPE [44–46].

3.2. Characteristics of porous activated carbons

3.2.1. BET surface area and pore size analysis

The surface area and porosity parameters for all AC powders (SAC, HAC and EAC) have been comparatively discussed by recording the measurements through N_2-adsorption desorption isotherms, as shown in Fig. 3 (A). According to IUPAC classification, all three AC powders exhibit Type-IV isotherms [47], although the shape of the HAC isotherm could be also ascribed to Type I. The initial rapid increase behaviour in the adsorbed N_2-gas at relative pressure $P/P_0 < 0.004$ to 0.006, present in all the isotherms (SAC, HAC and EAC), is related to single layer adsorption in the micropores of the carbon materials. Moreover, the progressive increase in the gas adsorption in the range of relative pressure $0.004 < P/P_0 < 0.5$ indicates that the AC samples contain pores with polydisperse size, from micropores to mesopores [39,42,47]. The quantitative analysis of different parameters calculated from the BET analysis, such as BET surface area and pore volume, is listed in Table 1 for all the AC materials. The STSA and the micropore surface area for all three powders (SAC, HAC and EAC) are reported in Table 1. The detailed discussion and calculations about STSA can be found in the supporting

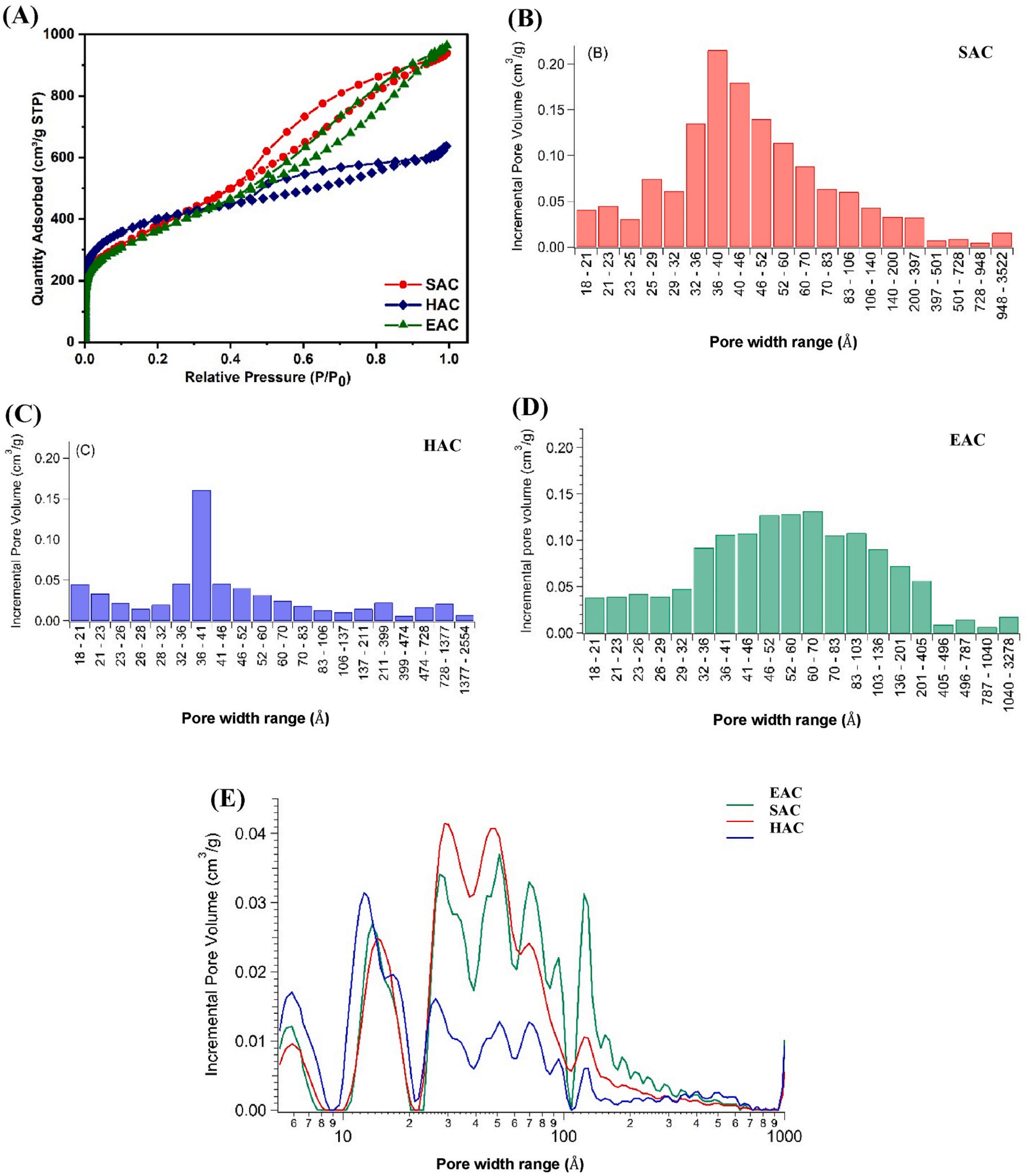

Fig. 3. (A) N_2- adsorption-desorption isotherms of all ACs, (B–D) Pore size distributions obtained by BJH method (E) Pore size distributions by NL-DFT method.

Table 1
Surface area and pore volume values for all the AC materials.

AC Material	Biomass: $ZnCl_2$ (w/w) ratio	BET surface area (m^2 g^{-1})	Pore volume (cm^3 g^{-1})	STSA (m^2 g^{-1})	Micropore surface area (m^2 g^{-1})
SAC[a]	1:2	1238	1.4	1125	185
HAC[b]	1:2	1459	0.6	500	959
EAC[c]	1:2	1381	1.3	1360	21.2

[a] AC prepared from raw material followed by activation.

[b] AC prepared from hydrothermally pre-treated raw material at ~300 °C before activation.

[c] AC prepared from ethanal soaked raw material for ~20 days before activation.

information. It is worth noting that HAC features the highest specific surface area and the highest micropore surface area among the three samples.

Type-IV isotherms of porous carbon materials can be further classified into different types of Hysteresis loops [47]. In the present case, the SAC and EAC isotherms show hysteresis loop of H3-type while HAC isotherm can be classified as hysteresis loop of H4-type [47], as shown in Fig. 3 (A). HAC is characterized by a smaller hysteresis loop as compared to the SAC and EAC, because of its different ratio of mesopores to micropores volume [30] and in particular due to the highest percentage of micropores.

These results can be explained by considering that the hydrothermal pretreatment with $ZnCl_2$ partially breaks the lignin polymer present in the biomass, causing structural changes and promoting the formation of a lignin-Zn complex, thus increasing its vulnerability to carbonization [30,48]. Furthermore, the hydrothermal pretreatment has an impact on cellulose fibers, and the presence of $ZnCl_2$ as an activating agent helps the swelling and the partial depolymerization of cellulose [30,48]. This makes the cellulose chains more accessible and increases the availability of more reactive sites for the subsequent carbonization step. Additionally, $ZnCl_2$ causes the hydrolysis and solubilization of the hemicellulose components, releasing sugars and other soluble fragments [48]. Hemicellulose residues increase the porosity of the activated carbon and aid the production of carbonaceous materials during carbonization [29,48]. During this step, the presence of $ZnCl_2$ and of hydrothermally pretreated residues acts as catalysts, promoting the activation of carbon precursors and the creation of oxygen-containing functional groups on the carbon surface, which improve adsorption capacity and electrochemical performance of ACs [29,39].

Another pre-treatment step is the ethanol soaking of raw biomass (EAC) for longer duration (about 20 days). This soaking process before activation facilitates the partial dissolution of lignin, favoring its removal and improving cellulose and hemicellulose accessibility [30,48]. After soaking in ethanol, the cellulose fibers swell, losing their crystalline structure and becoming more vulnerable to heat degradation [29,30]. Furthermore, the ethanol soaking solubilizes and partially removes hemicellulose, which disrupts the structure of the cell wall and facilitates further processing [29,30,47].

Among all the samples, HAC is characterized by the highest BET surface area. This is due to the hydrothermal pretreatment of the biomass in water at relatively moderate temperature under autogenous pressure. This treatment leads to the breakdown of the biomass structure and the formation of a carbon-rich material, often referred to as hydrochar, which introduces some degree of porosity into the material and, more importantly, it enhances the susceptibility of the biomass to subsequent activation processes.

Pore size distributions obtained by BJH model applied to the desorption brand are displayed in Fig. 3(B–D). The distribution of the EAC sample appears quite polydisperse, mostly in the 2–40 nm range. In SAC the distribution appears polydisperse in the same broad range but shows a defined maximum around 4–5 nm. Finally, HAC displays a well-defined preferential pore size centered around 4 nm.

In Fig. 3 (E) the distributions obtained by DFT model are reported, to highlight the micropore range. The comparison of the three curves shows that all the three samples contain a fraction of pores with size around 6 Å and another distribution around approximately 14 Å, in addition to the mesopore distribution. In the HAC sample, the incremental pore volume of the micropores is significantly higher than that of the mesopores. Conversely, in the SAC and EAC samples, the mesopores have a higher incremental pore volume than the micropores.

3.2.2. *SEM images*

SEM images of all the prepared AC powders were acquired to confirm the surface morphology, as shown in Fig. 4. All ACs show distinct pores with irregular shape and size. The pre-treated ACs (HAC and EAC) show smaller pores (nanometer size) with respect to SAC, and a dense distribution in a certain area, which confirms the higher surface area discussed in BET section Fig. 4(C–F). Moreover, significant uniform surface structure and pore distribution in HAC powder, as compared to other ACs, can been noticed in Fig. 4(C–D), which is the reason for the optimized performance of HAC-based EDLC, discussed later in the electrochemical section.

3.2.3. *XRD and Raman analysis*

Fig. 4 (G) shows the XRD patterns for the obtained activated carbon powders; all exhibit similar features characterized by two predominant wide peaks around ~25° and ~43.4°, which relate to (002) and (100) graphitic planes, respectively [42]. The second broad and small peak between 40° and 48° indicates that all three samples possess less developed intra graphitic layers [42]. In conclusion, all three carbon powders show two broad reflections and absence of any sharp peak in their XRD patterns suggesting that the activated carbon powders prepared through different synthesis routes possess highly disordered nature, i.e. low level of crystallinity in their graphitic domains [30].

Structural information for all three carbon materials (SAC, HAC and EAC) was acquired by recording Raman spectra, as shown in Fig. 4 (H). To better compare the samples, in Figs. S3–4 † the spectra were normalized and divided between low and high wavenumbers. All AC powders exhibit two typical prominent bands around ~1350 cm^{-1} and ~1590 cm^{-1} that are correlated with D and G-bands, respectively. The D band, also known as the disorder peak, is caused by the breathing modes of sp^2 carbon atoms in rings with structural defects or disorder, such as vacancies, edge defects, and non-six-membered rings [30,49]. The existence of the D band indicates structural disorder or flaws within the structure [49]. These flaws can result from a variety of processes, such as incomplete graphitization, functionalization, or surface alteration [42,49]. The G band or graphitic peak represents in-plane vibrational modes of sp^2 carbon atoms in a graphitic lattice structure [50]. This indicates the presence of organised, crystalline domains in the carbon substance [50,51]. Other contributions were highlighted by the bands deconvolution (Fig. S5 †). By the ratio I_D/I_G of the integrated areas of the D and G bands, the values of 2.0 ± 0.2 (SAC), 1.6 ± 0.2 (HAC) and 1.7 ± 0.2 (EAC) are in agreement with the nanometric size of the crystallites.

Additionally, all the ACs' Raman spectra present two clear broad bands centered at ~2700 cm^{-1} and ~2940 cm^{-1} denoting 2D and D + G bands respectively. The 2D band indicates the presence of many graphene layers or graphitic domains in the AC, while the D + G bands reflect the coexistence of defects in structure and organised graphitic areas in the carbon material [49,50,52].

3.3. *Performance study of supercapacitors/EDLCs*

3.3.1. *Electrochemical impedance spectroscopy (EIS) studies*

To evaluate bulk and charge transfer resistances and capacitive behaviours for all the EDLCs (Cell @1, Cell @2 and Cell @3), the EIS spectra of each cell in the frequency range of 10 mHz–100 kHz was acquired. The Nyquist plots i.e., real versus imaginary impedance (Z'

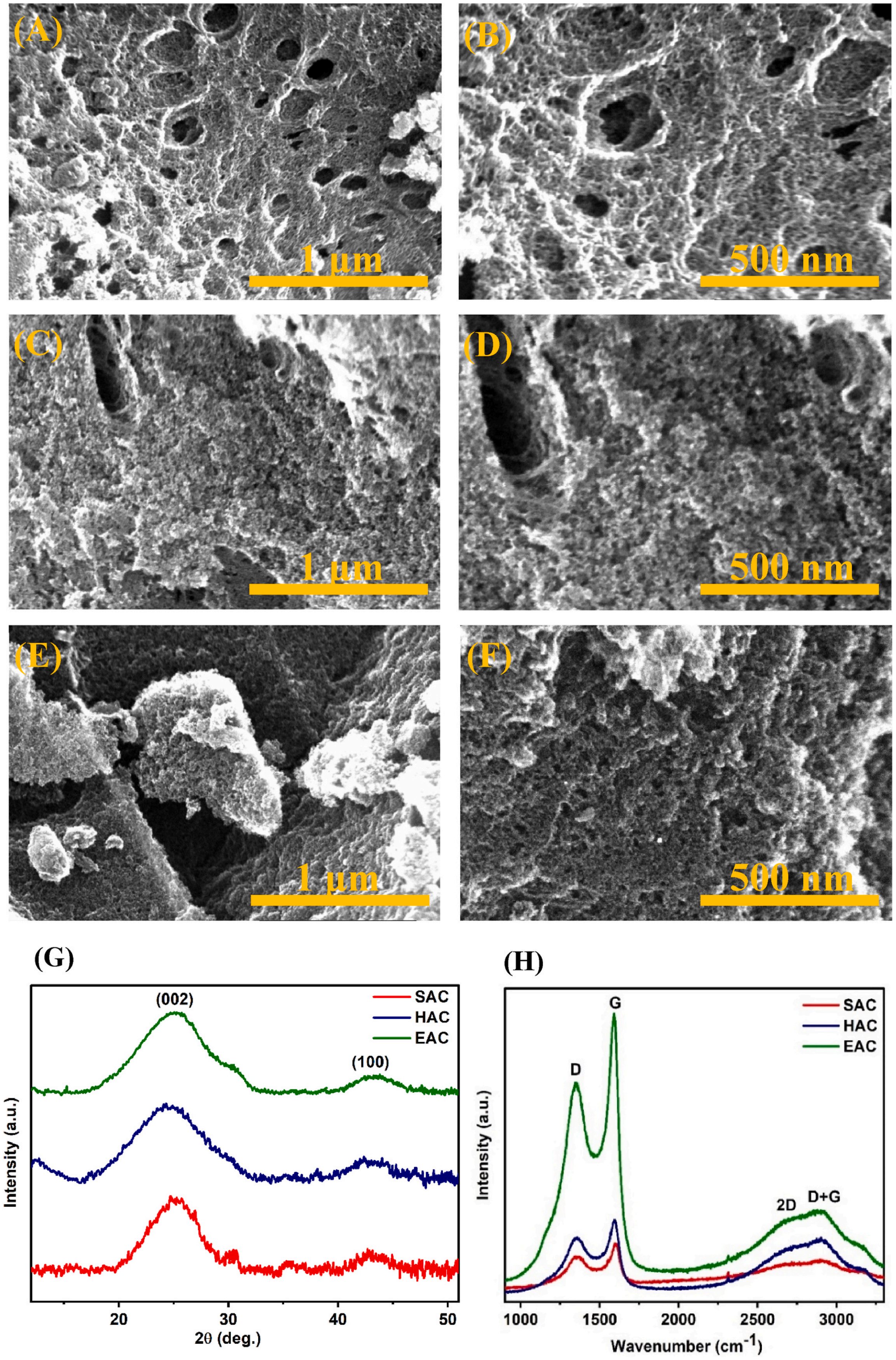

Fig. 4. SEM images of all ACs namely, (A–B) SAC, (C–D) HAC and (E–F) EAC (G) Powder X-ray diffraction and (H) Raman spectra of activated carbon powders (SAC, HAC and EAC).

versus -Z”) at varying frequencies, for each are shown in Fig. 5 (A-C). All the cells exhibit a rising straight line, indicating a dominant capacitive behaviour. Moreover, to better understand the process, the mid to high frequency range of the Nyquist plot has been expanded, as shown in the insets of Fig. 5 (A-C). All the cells exhibit a semicircular arc in this region which has two intercepts at real impedance axis, namely bulk resistance (R_b) and charge-transfer resistance (R_{ct}) at the electrode-electrolyte interface, denoted by arrows in the insets of Fig. 5 (A-C). R_b is mainly

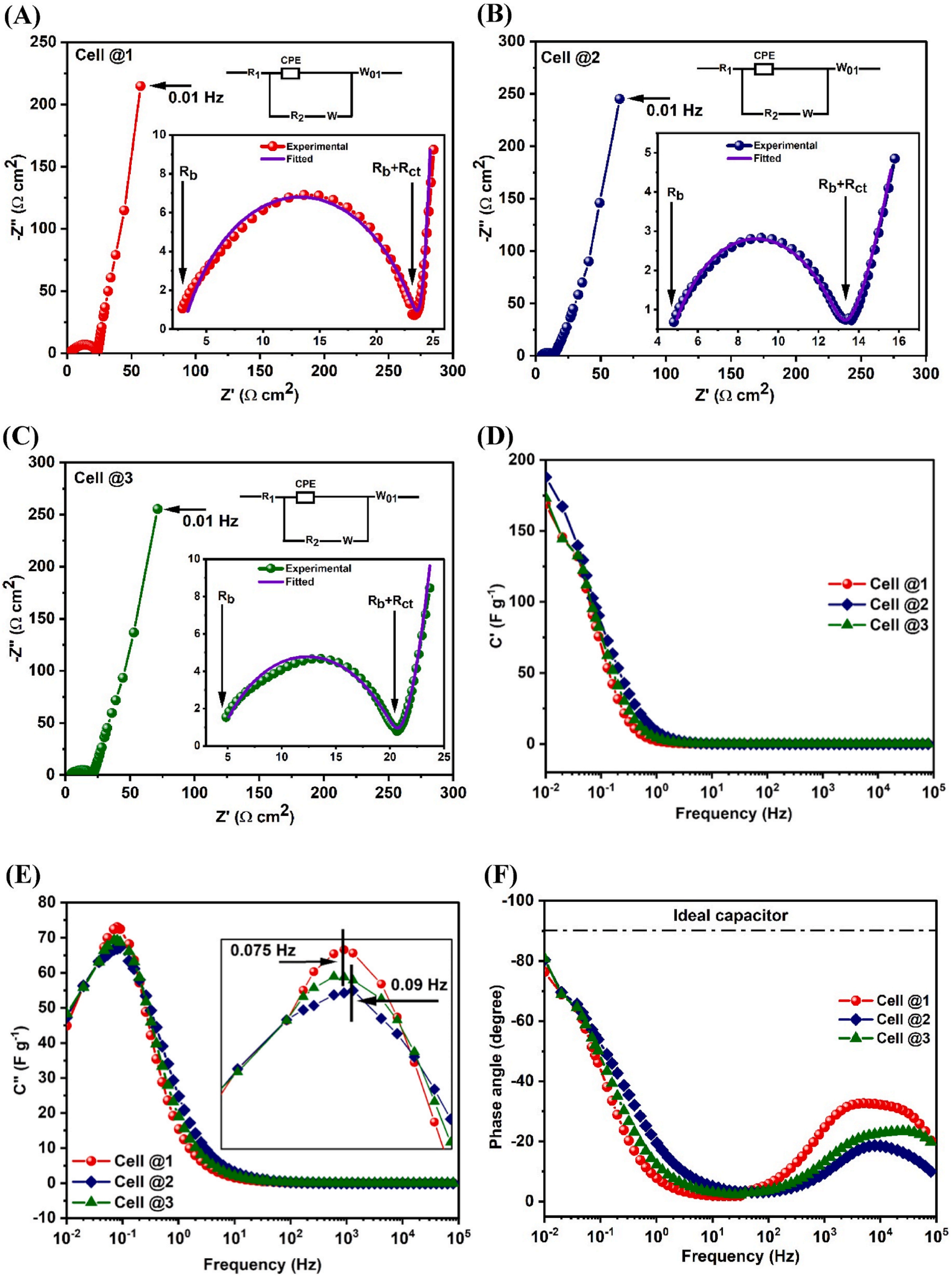

Fig. 5. EIS (Nyquist) plots of EDLC cells (A) Cell @1, (B) Cell @2, (C), Cell @3 in frequency range from 100 kHz to 10 mHz (expanded EIS plot in high frequency region and equivalent circuit are also shown in the respective figure), (D) real values of capacitance C′, (E) imaginary values of capacitance C″, and (F) phase angle versus frequency plots for all the cells.

related to the bulk electrolyte resistance, excluding the AC electrodes resistance, while R_{ct} is related to the resistance provided by the faradic/redox reactions between the electrolyte ions and the surface functionalities present in the carbon materials surface [41,53].

The values of the specific capacitance (C_{sp}) for all the cells have been calculated by the formula $C_{sp} = 2/(2\pi f \times m \times |Z''|)$, where (m) is the mass of the active material in the single electrode, ($|Z''|$) is the magnitude of the imaginary component of the impedance, which has been calculated at the frequency $f = 0.01$Hz [41]. The electrical parameters for all the cells, such as R_b, R_{ct} and R (resistance Z' at frequency 0.01 Hz) have been listed in Table 2. All the cells possess similar values of resistive parameters including R_b and R. Similar values of R_{ct} indicate that all the carbon materials possess same types of surface functional groups responsible for the faradic charge-transfer reactions at the interface. Moreover, slightly higher value of the C_{sp} for the Cell @2 (HAC based carbon electrodes), with respect to the Cell @1 and Cell @3, is achieved due to the moderately higher BET specific surface area of HAC (hydrothermally pre-treated raw powder before activation) as compared to SAC and EAC, a s discussed in Table S6 †.

To better understand the accuracy of electrical parameters R_b and R_{ct}, EIS data has been fitted in the mid to high frequency region with the equivalent circuit represented in the insets of Fig. 5 (A-C). Different circuit elements have been used to achieve a better fit of the EIS data. The fitted resistive parameters R_1 and R_2, constant phase element (CPE) and Warburg parameters (W and W_{o1}) for each cell are listed in Table S6 † [54]. The Warburg parameters are mainly related to the diffusion/-transport of the electrolyte ions (Li^+, EMI^+, Tf^-) in the pores of the carbon electrodes; the detailed information about the EIS spectra fitting can be found in recent literature [41,54]. The accuracy of fitted equivalent circuit employed for each cell can be observed by comparing the fitted resistive parameters R_1 and R_2 with the experimental values R_b and R_{ct} which are almost identical.

To extract information about the ion-diffusion mechanism for each cell, the real and imaginary capacitance values (C' and C'') have been plotted against the frequency in the range of 10 mHz–100 kHz, as represented in Fig. 5 (D-E). The values of C' and C'' can be evaluated by incorporating the real and imaginary impedances (Z' and Z") in the following formula [55]:

$$C'(\omega) = \frac{-Z''(\omega)}{\omega|Z(\omega)|^2} \tag{2}$$

$$C''(\omega) = \frac{Z'(\omega)}{\omega|Z(\omega)|^2} \tag{3}$$

From the real capacitance C' versus frequency plot shown in Fig. 5 (D), all the cells exhibit similar behaviour over a wide frequency range. For each cell the C' value, calculated in the low frequency region at 0.01 Hz, is consistent with the capacitance calculated from GCD analysis, discussed later in this work. C' values in the high frequency range (10–100 kHz) are almost negligible, strongly suggesting the negligible capacitive behaviour in the high frequency range [30]. The expected strong capacitive behaviour in the lower frequency range i.e. < 10 Hz can be observed in addition to the saturation behaviour at very low frequency <0.1 Hz. Moreover, slightly greater values of capacitance C' can be observed for Cell @2, which indicates more suitable porosity and surface area of the carbon electrodes due to the hydrothermal pre-treatment before activation, with respect to the other activation methods.

Fig. 5 (E) shows C'' as a function of frequency. A peak can be observed in the frequency range 0.01–100 Hz for each cell. The peak of C'' is located at a frequency f_0 which is related to the relaxation frequency [29,30]; the values of f_0 for Cell @1, Cell @2 and Cell @3 are 0.075 Hz, 0.075 Hz and 0.09 Hz respectively. For each cell the transition between capacitive to resistive behaviour can also be studied as C" values correspond to below and after f_0 values. HAC shows a slight increase value of f_0 which indicates that ions have more space for facile movement, due to the suitable pore size distribution which leads to a better electrode performance [29,30]. For each cell, the ideality of the device has also been judged with a phase angle versus frequency graph. The phase angle plot, shown in Fig. 5 (F), confirms the capacitive behaviour in the lower frequency range (<10Hz), as discussed above. All three cells show phase angle values around 80° at low frequencies, which is close to the phase angle value of an ideal supercapacitor (90°), represented by dotted line in Fig. 5 (F).

Table 2

Electrical parameters evaluated from EIS studies for supercapacitors.

EDLCs	R_b (Ω cm^2)	R_{ct} (Ω cm^2)	R (Ω cm^2)
Cell @1	2.7–2.9	18–21	55–60
Cell @2	4.5–4.8	9–17	58–64
Cell @3	4.7–5	12–19	62–69

3.3.2. *Cyclic voltammetry*

All the EDLC cells (Cell @1, Cell @2 and Cell @3) have been characterized in a two-electrode configuration by means of CV in the potential range from 0 to 2.5 V. Comparative CV curves for all three cells are shown in Fig. 6 (A), to study the cell in terms of capacitance, performance, and rate capability. The CV patterns show that the pre-treatment methods (HAC and EAC) improved the electrochemical performance of the carbon materials: higher voltametric currents are observed for Cell @2 and Cell @3 with respect to Cell @1. Moreover, further comparison shows that HAC-based cell (Cell @2) is characterized by a slightly higher capacitance (174 F g^{-1} while EAC based cell has 165 F g^{-1}) and a more rectangular, box-like structure, indicating lower resistance than EAC electrodes thanks to a more suitable porosity, a more suitable pore size and a slightly higher BET surface, which facilitates ion mobility.

Fig. 6 (B) shows the CV curves of Cell @2 for varying voltage ranges from 0 to 2.5 V at a constant scan rate of 10 mV s^{-1}. The CV patterns for the other cells (Cell @1 and Cell @3) have also been recorded for the same potential ranges 0–2.5 V and shown in Figs. S7 and S9 †. The typical, box-like rectangular shape (typical of an ideal supercapacitor) of CV curve is maintained up to the voltage 2.3 V, after which curves start deviating from the ideal shape, indicating a resistive behaviour; consequently, the cells can be considered electrochemically stable in the voltage range of 0–2.3 V, and for further studies all the cells have been tested in this stable working voltage window range. Furthermore, this stable voltage window has also been confirmed for all the cells from the GCD analysis, which is discussed later.

The scan rate stability for all the cells (Cell @1 to Cell @3) has been tested for varying scan rates from 10 to 300 mV s^{-1}, as shown in Fig. 6 (C) for Cell @2. For other cells the CV patterns with varying scan rates are shown in Figs. S8 and S10 †. The CV curves can maintain their rectangular box-like shape up to the scan rate of 100 mV s^{-1}, deviating for higher scan rates, which shows that all the cells have moderate rate capability. The fast ion (Li^+, EMI^+, Tf^-) movements through the pores of ACs even at higher scan rates determines the moderate rate capability of the cells.

The specific capacitance (C_{sp}) dependence from the scan rate, ranging from 10 to 300 mV s^{-1}, is shown in Fig. 6 (D). Specific capacitance (C_{sp}) with varying scan rates was calculated from the following equation:

$$C_{sp} = \frac{2 \times j}{s \times m} \tag{4}$$

where j is the current density at the middle of the voltage range, s is the scan rate (mV s^{-1}) and m is the mass on a single electrode [30].

Each cell shows an initial fast decrease in capacitance, which is later followed by gradual decrease in the C_{sp} value. Such behavior can be

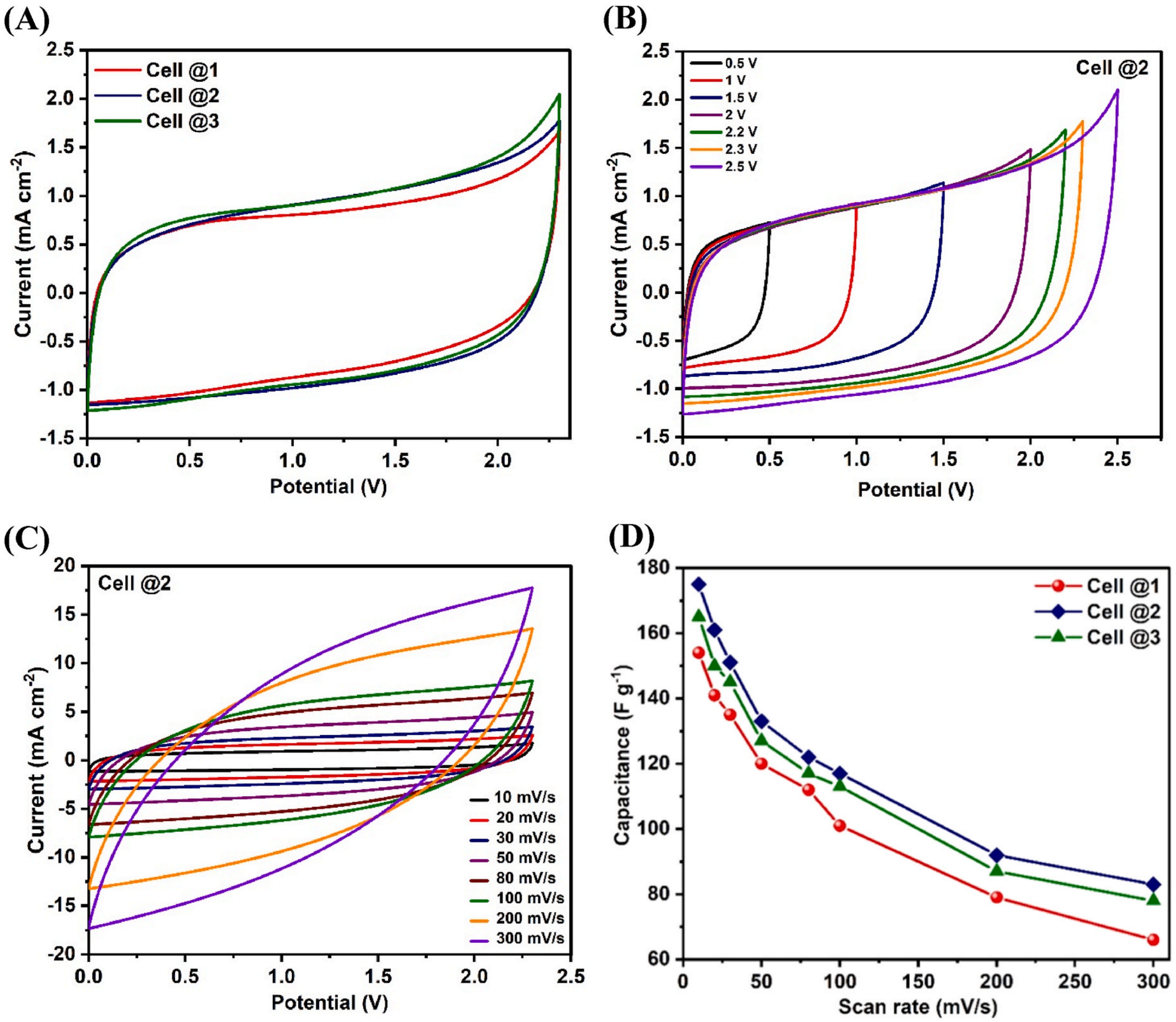

Fig. 6. (A) Comparative CV patterns of all the cells in the optimized voltage range from 0 to 2.3 V, (B) CV response of Cell @2 with varying voltage ranges recorded at the scan rate of 10 mV s^{-1}, (C) CV patterns measured at different scan rates from 10 to 300 mV s^{-1} for Cell @2, (D) specific capacitance (C_{sp}) versus scan rate plot for all the EDLC cells.

explained as follows: at lower scan rates the ions diffuse completely inside the pores of the carbon electrodes, which leads to increase in the charge storage mechanism, hence in enhanced C_{sp} values [29,30], while at higher scan rates the ions are not completely absorbed/desorbed in the pores due to faster dynamics, which leads to lower capacitance.

3.3.3. Galvanostatic charge-discharge

Charge-discharge tests have been carried out on EDLCs based on different ACs (SAC, HAC and EAC), to evaluate different parameters such as specific capacitance, energy, and power density. A comparative GCD graph for all the cells (Cell @1 to Cell @3) recorded at 1 A g^{-1} are shown in Fig. 7 (A). It can be observed that all cells exhibit almost triangular GCD curves (as expected for ideal supercapacitors), indicating a proper electric double layer formation at the interface [30]. Moreover, Cell @2 performs better than Cell @1 and Cell @3 by having slightly larger discharge time, which suggests better charge double layer formation, which leads to higher capacitance values [53].

The internal resistance or equivalent series resistance (ESR) for all the cells have been calculated by measuring the instant voltage drop (ΔV) in the discharge curve after the current reversal (j), using the following equation [53]:

$$\mathrm{ESR} = \frac{\Delta V}{2j} \tag{5}$$

The values of ESR and specific capacitance C_{sp} from the discharge curve have been calculated for each cell and listed in Table 3. The value of the C_{sp} for each cell have been calculated from the equation mentioned below [29,30]:

$$C_{sp} = \frac{4\,j \int V\,dt}{m \times V^2\big|_{V_i}^{V_f}} \tag{6}$$

where (j) is the current density, m is the mass of active material on a single electrode, $\int V\,dt$ is the area under the discharge curve, V is the maximum operating voltage, and V_i and V_f are the initial and final values of GCD curves voltages [29,54,56,57].

The effect of the pre-treatments (HAC and EAC) before activation on ACs can be observed, as Cell @2 and Cell @3 show slightly lower values of ESR, respectively of 21-19 and 24–30 Ω cm^2, as compared to Cell @1, with an ESR of 22–30 Ω cm^2. This indicates better and faster mobility of ions at the interface, which leads to higher capacitance. Substantially higher capacitance, up to 161–170 F g^{-1}, as compared to Cell @1 with 135–148 F g^{-1} and Cell @3 with 153–158 F g^{-1}, and lower ESR value of Cell @2 are the consequence of suitable porosity, higher specific surface area and appropriate amount of mesoporosity in the HAC powder. The appropriate amount of mesoporosity acts as a faster transport route for ions at the interface.

Fig. 7 (B) shows charge-discharge profiles of Cell @2 in the varying

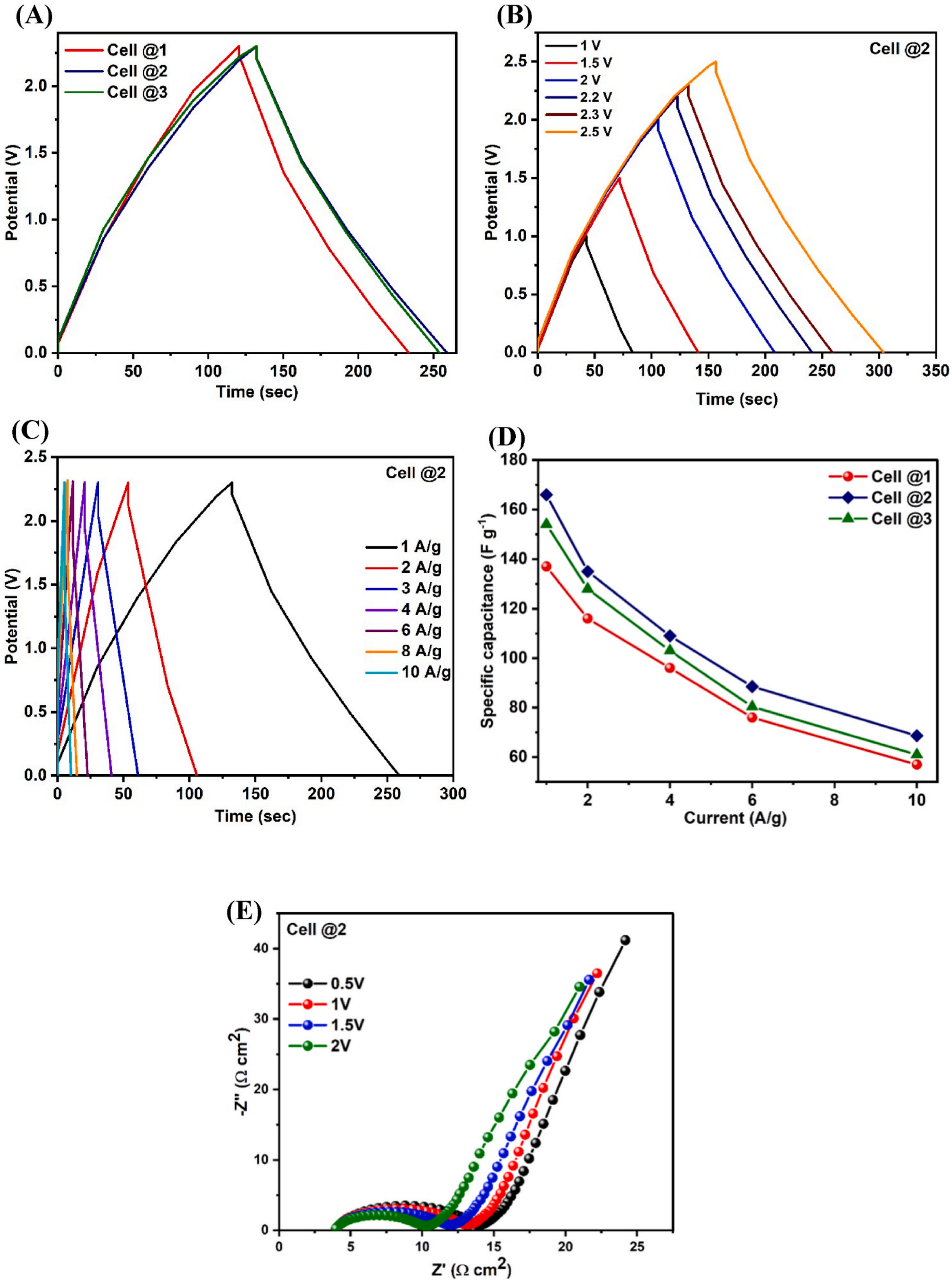

Fig. 7. (A) Comparative GCD curves for all the cells in the optimum voltage range 0–2.3 V and, (B) GCD curves of Cell @2 with varying voltage ranges recorded at current density 1 A g^{-1}, (C) GCD curves measured at different current densities from 1 to 10 A g^{-1} for Cell @2, (D) specific capacitance (C_{sp}) versus current density plot for all the EDLC cells, (F) impedance spectra of Cell @2 at different voltages.

range of potential 0–2.5 V at 1 A g^{-1}. For Cell @1 and Cell @3 the charge discharge curves are shown in Figs. S11 and S13 †. Each cell shows almost linear charge-discharge curves up to the potential 2.3 V; at higher voltage, GCD curves start deviating from ideal behaviour. Almost linear behaviour up to 2.3 V proves electrostatic charge-storage mechanism at the interface [29]. This suitable electrochemical window has been confirmed in CV analysis.

GCD curves at varying current densities from 1 to 10 A g^{-1} in the

Table 3
Parameters evaluated from GCD analysis for all three cells at a constant current density 1 A g^{-1}.

EDLCs	ΔV (V)	ESR (Ω cm^2)	C_{sp} (F g^{-1})	Esp (Wh kg^{-1})	P_{eff} (W kg^{-1})
Cell @1	0.07–0.08	22–33	135–148	24–26	790–805
Cell @2	0.85–0.9	21–29	161–170	29–31.34	839–860
Cell @3	0.9–0.1	24–30	153–158	28–29.5	803–828

potential range 0–2.3 V is shown for Cell @2 in Fig. 7 (C). For other cells (Cell @1 and Cell @3) similar GCD curves are shown in Figs. S12 and S14 †. From the GCD curves at higher current densities (8–10 A g^{-1}) it is evident that the cells are able to maintain their linear charge-discharge profiles.

Fig. 7 (D) shows the variation of the specific capacitance (C_{sp}) values for each cell with respect to the current densities from 1 to 10 A g^{-1} which gives information about the rate capabilities of each device. For all cells, an initial fast fading in C_{sp} values of about 35 % is noticeable up to a current density of 4 A g^{-1}; for higher current densities a progressive decrease in C_{sp} values can be observed, up to 10 A g^{-1}. Pre-treatments, namely hydrothermal and ethanol soaking before activation of the biomass waste, determine improved rate performance for the entire range of the current densities; almost parallel curves are shown in Fig. 7 (D) for each cell. Further comparison shows that Cell @2 has higher rate performance for the entire range of the current density up to 10 A g^{-1} as it has highest C_{sp} values.

The EIS spectra at different applied voltages have been recorded for all the cells, as shown in Fig. 7 (E) for Cell @2. For Cell @1 and Cell @3 the EIS spectra have been reported in Figs. S15 and S16 †, respectively. All the curves exhibit reduced R_{ct} values as voltage increases as well as slightly different diffusion curves at lower frequency. From this analysis, it can be concluded that all cells exhibit mixed capacitive and resistive/diffusive behaviour, with potential pseudocapacitive contributions [58]. This typical behaviour is observed in the activated carbons based SCs where the charge transfer (pseudocapacitive behaviour) is observed due to the surface functionalities such as hydroxyl, carboxyl, phenol, and carbonyl adsorbed on the large-surface-area AC electrodes [59–61]; these reactions cause a pseudocapacitive contribution, resulting in an increase in capacitance.

The values of specific energy (E_{sp}) and effective power density (P_{eff}) for each cell have been calculated from the following equations [53]:

$$E_{sp} = \frac{j \times \int V\,dt}{2\,m} \tag{7}$$

$$P_{eff} = \frac{E_{sp}}{\Delta t_{dis}} \tag{8}$$

where j is the current density, m is the mass of active material employed on a single electrode, $\int V\,dt$ is the area under the discharge curve, and Δt_{dis} is the discharge time [53]. The parameters evaluated at 1 A g^{-1} for each cell have been listed in Table 3. A significant improvement in the E_{sp} and P_{eff} can be observed for the Cell @2 and Cell @3, which further indicates the benefits of pre-treatment steps before activation on carbon powders. Furthermore, Cell @2 shows optimum performance by owing higher values of specific energy and power as compared to Cell @3 since HAC powder has optimum BET surface area and suitable pore size distribution for high performance EDLC.

Table 4 shows a comparison between the characteristics and performance of the supercapacitors prepared in this work and those of other EDLCs derived from different biomass wastes, reported in recent literature. The comparison shows that the devices prepared in this work (supercapacitors based on melon waste carbon electrodes) boast almost equal or even better performance as compared to the other EDLCs in terms of specific capacitance, energy, and power density.

The Ragone plot for the three cells has been represented in Fig. 8 (A). All the cells (Cell @1 to Cell @3) show typical EDLC behaviour, as an increase in specific energy values can be seen at the cost of decreasing values of effective power. The optimum performance of Cell @2 can also be appreciated since it clearly displays a higher value of effective power and specific energy (parallel curve with respect to the other cells) in comparison with other EDLCs. Moreover, Cell @2 shows an 8-fold increase in the effective power from ~0.9 to ~7 kW kg^{-1} at the expense of specific energy from ~30 to 12 Wh kg^{-1}, which shows quite great performance from EDLC point of view. The long cyclic charge-discharge curve up to 8000 cycles for all the cells, recorded at 1 A g^{-1}, are shown in Fig. 8 (B). The Coulombic efficiency (η%), which has been evaluated from the equation [54]:

$$\eta = \frac{t_D}{t_C} \times 100\ \% \tag{9}$$

where t_D and t_C are the discharging and charging time, respectively and specific capacitance (C_{sp}), is shown as a function of cycles, up to 8000 cycles, in Fig. 8 (B). Cell @2 shows optimum performance by having larger values of capacitance throughout the 8000 cycles in comparison with the other cells. As evident from Fig. 8 (B), Cell @2 shows the initial

Table 4
Comparison of EDLCs prepared with different biomass derived AC based supercapacitors.

Biomass Precursor	Pre-activation treatment	Activating agents	Surface area (m^2 g^{-1})	Specific capacitance (Fg^{-1})	Specific energy (Wh kg^{-1})	Specific power (kW kg^{-1})	Ref.
Corn Stover	Pyrolysis	KOH	2441	398 at 0.5 A g^{-1}	5.01	0.1	[62]
Cottonseed meal	Hydrothermal treatment	K_2CO_3	2361	71.8 at 0.5 A g^{-1}	34.4	0.225	[63]
Bamboo	NA	K_2CO_3	1802	–	–	–	[64]
Banana stem fibers	NA	$ZnCl_2$	788.09	179	6.19	0.044	[65]
Peanut shell	NA	$ZnCl_2$	1549	333 at 0.5 A g^{-1}	8.5–4.6	0.1–6.56	[66]
Pinecone	NA	$ZnCl_2$	1781	255 at 1 mA cm^{-2}	20	0.055	[67]
Pollen cone	Pre-carbonized	KOH	2314	146 at 0.5 A g^{-1}	21	0.19	[42]
Rice straw	Pre-carbonized	KOH	2651	324 at 0.5 A g^{-1}	48.9	0.75	[68]
Tabacco waste	Hydrothermal treatment	KOH	1875.5	356.4 at 0.5 A g^{-1}	10.4	0.3	[69]
Corncob	NA	Steam	1210	120 at 1 A g^{-1}	5.3	8.276	[70]
Coffee bean	NA	H_3PO_4	742	160 at 1 A g^{-1}	15	0.075	[71]
Cotton stalk	NA	H_3PO_4	1481	114 at 0.5 A g^{-1}	–	–	[72]
Melon waste	Hydrothermal treatment	$ZnCl_2$	1459	161 - 170 at 1 A g^{-1}	29–31.34	0.84–0.86	**This work**
	Ethanol soaking treatment	$ZnCl_2$	1381	153–158 at 1 A g^{-1}	28–29.5	0.8–0.83	

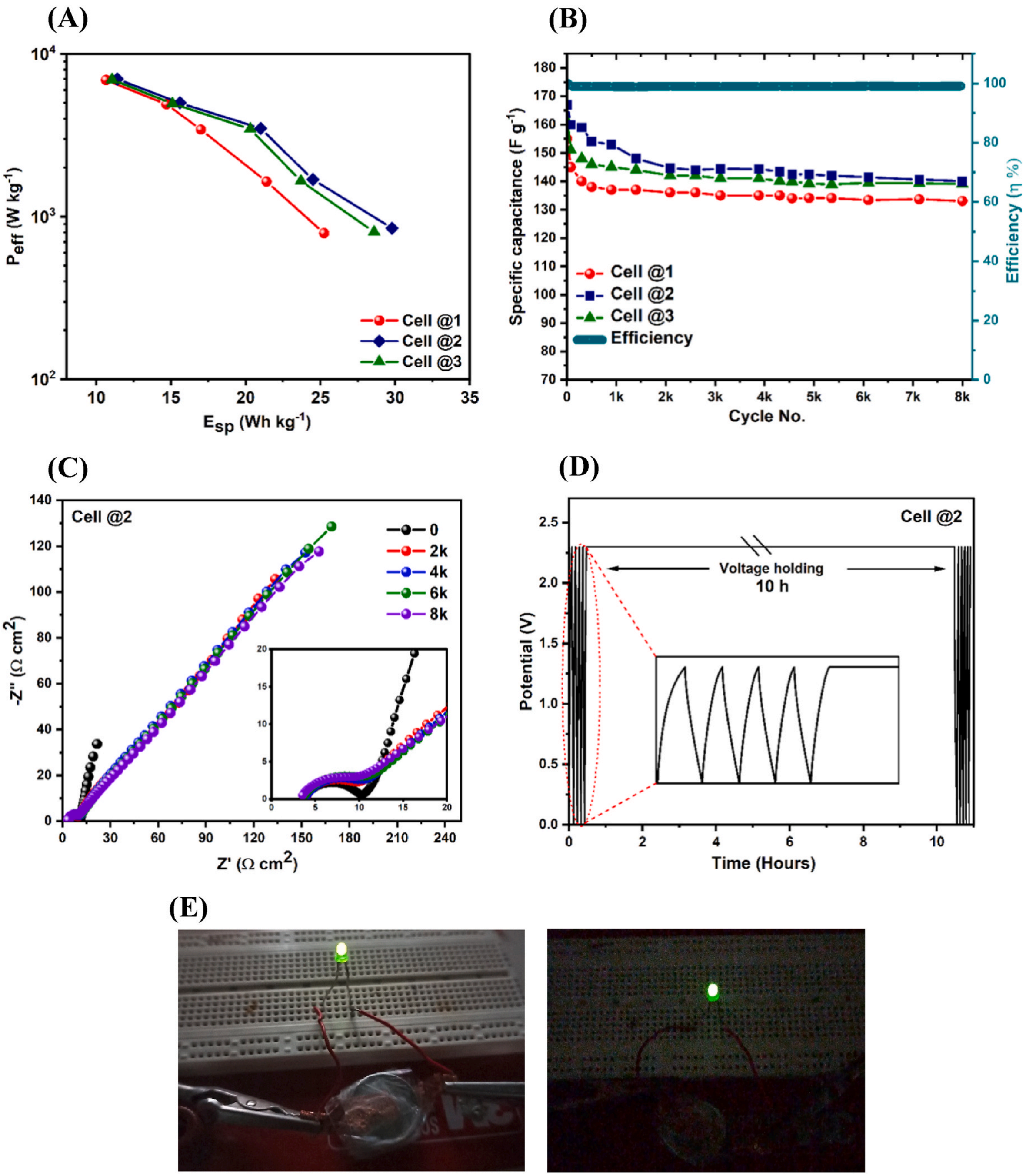

Fig. 8. (A) Comparative Ragone plots of all the cells (Cell @1 to Cell @3), (B) Coulombic efficiency and specific capacitance as a function of cycle number, recorded at a 1A g^{-1}, (C) EIS spectra of Cell @2 measured at different GCD cycling tests, (D) Floating test experiment for Cell @2 with 5 cycles of charge/discharge before and after 10 h of voltage holding, (E) Glowing LED by connecting three cells (Cell @2) in series.

~15 % fast capacitance fading after ~2000 cycles and then very slow fading up to 8000 cycles. The initial fast fading in the C_{sp} values is possibly due to the irreversible reactions between the surface functional groups in the activated carbons and electrolyte ions [42]. After ~2000 cycles, after the electrochemical reactions reach stability, further capacitance fading is gradual and can be related to the slowly blocking of micropores in the carbon material [42]. After some micropores are blocked the Coulombic efficiency also reaches almost 100 % which can be observed from Fig. 8 (B). The capacitance fading has been confirmed from the impedance plot by recording EIS at different GCD cycling tests, as shown in Fig. 8 (C) for Cell @2. For Cell @1 and Cell @3, the impedance spectra at different GCD cycling tests have been reported in Figs. S17 and S18 †, respectively. The significant initial and afterwards slow fading in capacitance indicates the higher value of imaginary impedance (Z″). Moreover, a slight increase in the charge transfer resistance R_{ct} can be observed, especially visible between the 0 cycle to the 2000 cycles spectra, but also observable for subsequent spectra. This effect can be due to a slight loss of contact between the electrode and the GPE; this becomes less observable at high cycle number and could probably be reduced by applying a higher pressure to the cell.

The stability of Cell @2 has also been tested with floating test experiments, by performing charge/discharge tests at 1 A g^{-1} of 5 cycles before and after 10 h of voltage holding, as mentioned in Fig. 8 (D) [73]. The specific capacitance have been calculated from the discharge curve of 3rd cycle before and after voltage holding. A ~27 % decay in specific capacitance has been noticed after 10 h of voltage holding at 2.3 V, which is quite good from an electrochemical point of view. In terms of application, a 30–50 mW green LED was lit up (in presence of dark and bright light atmosphere) for about 100–120 s by connecting three Cell @2 in series, as shown in Fig. 8 (E). This demonstrates the applicability of supercapacitors prepared here.

4. Conclusions

Hierarchical large surface area porous activated carbons were synthesized from melon peels waste. The starting material was processed and activated by means of $ZnCl_2$ and CO_2. The AC powders were analyzed through morphological, spectroscopic, BET surface area and porosity measurements. These activation processes led to the partial degradation of the lignin, cellulose and hemicellulose content, increasing the activation and thus the accessibility of the surface by the ions; in particular, the HAC sample showed slightly better performance by featuring a larger surface area and an appropriate amount of micro and mesoporosity. The prepared carbon electrodes were tested with a GPE containing 1 M LiTf in EMITf hosted in a PVdF-HFP polymer. The measured conductivity and ESW of the GPE are found to be $\sim 3.3 \times 10^{-3}$ S cm^{-1} and ~3.9 V versus Ag/Ag^{+} respectively, which is rather good for EDLC applications. Symmetric supercapacitors were assembled with the prepared ACs and GPE and characterized with the EIS, CV and GCD techniques. The stable working voltage window of EDLC cells was confirmed in the range from 0 to 2.3 V from both CV and GCD analysis. The HAC based EDLC shows better performance by having slightly higher capacitance values ~166 F g^{-1} as compared to the other EDLCs (EAC and SAC). Moreover, the optimized specific energy and power, calculated at 1 A g^{-1}, are 29–31 Wh kg^{-1} at power density of 839–860 W kg^{-1}, respectively. In summary, the HAC and EAC based EDLCs show slightly higher rate performance as compared to SAC based EDLC, as confirmed from the CV and GCD analysis; in particular, HAC-based cell is characterized by a better rate performance in comparison with the EAC based cell. Furthermore, the HAC based EDLC shows electrochemically stable performance up to 8000 cycles with initial 15 % capacitance fading and Coulombic efficiency close to 100 %.

CRediT authorship contribution statement

Niyaz Ahmad: Writing – original draft, Visualization, Validation, Methodology, Investigation, Formal analysis, Data curation, Conceptualization. **Alessia Rinaldi:** Investigation, Formal analysis. **Michele Sidoli:** Writing – original draft, Visualization, Validation, Methodology, Investigation, Formal analysis, Data curation, Conceptualization. **Giacomo Magnani:** Writing – original draft, Supervision, Resources, Methodology, Investigation, Conceptualization. **Vincenzo Vezzoni:** Visualization, Validation, Investigation, Formal analysis, Data curation. **Silvio Scaravonati:** Resources, Methodology, Investigation. **Lorenzo Pasetti:** Methodology, Investigation, Formal analysis. **Laura Fornasini:** Writing – original draft, Supervision, Methodology, Investigation. **Harsh Gupta:** Methodology, Investigation, Formal analysis. **Michele Tamagnone:** Supervision, Methodology, Investigation. **Francesca Ridi:** Writing – original draft, Supervision, Methodology, Investigation, Formal analysis. **Chiara Milanese:** Writing – original draft, Visualization, Validation, Supervision, Resources, Project administration, Methodology, Funding acquisition, Conceptualization. **Mauro Riccò:** Validation, Supervision, Resources, Project administration, Methodology, Conceptualization. **Daniele Pontiroli:** Writing – original draft, Visualization, Validation, Supervision, Resources, Project administration, Methodology, Funding acquisition, Conceptualization.

Declaration of competing interest

The authors declare that they have no known competing financial interests or personal relationships that could have appeared to influence the work reported in this paper.

Data availability

Data will be made available on request.

Acknowledgements

In this publication it was involved a researcher with a research contract co-financed by the European Union - PON Research and Innovation 2014–2020 pursuant to art. 24, paragraph 3, lett. a), of Law December 30, 2010, n. 240 and subsequent amendments and of the D.M. August 10, 2021 no. 1062. We also acknowledge and thank Cariplo Foundation for the financial support (project number 2019–2152, ‘Gaining health and energy from Lombard agrifood waste’), the National Recovery and Resilience Plan (NRRP), Mission 04 Component 2 Investment 1.5 – NextGenerationEU, call for tender n. 3277 dated December 30, 2021 (Award Number: 0001052 dated June 23, 2022) and the NRRP Mission 4 - Component 2 - Investment 1.1 ”Fondo per il Programma Nazionale di Ricerca e Progetti di Rilevante Interesse Nazionale (PRIN)” funded by the European Union - Next Generation EU, project PRIN2022-202278NHAM (PE11) CHERICH-C "Chemical and electrochemical energy storage materials from organic wastes: the treasure hidden in C based materials”. G. Cassi is acknowledged for the growing of the organic melons gifted for this research.

Appendix A. Supplementary data

Supplementary data to this article can be found online at https://doi.org/10.1016/j.jpowsour.2024.235511.

References

[1] A. Morenghi, S. Scaravonati, G. Magnani, M. Sidoli, L. Aversa, R. Verucchi, G. Bertoni, M. Riccò, D. Pontiroli, Asymmetric supercapacitors based on nickel decorated graphene and porous graphene electrodes, Electrochim. Acta 424 (2022) 140626, https://doi.org/10.1016/J.ELECTACTA.2022.140626.

[2] A.A. Hor, N. Yadav, S.A. Hashmi, Enhanced energy density quasi-solid-state supercapacitor based on an ionic liquid incorporated aqueous gel polymer electrolyte with a redox-additive trimethyl sulfoxonium iodide, J. Energy Storage 64 (2023) 107227, https://doi.org/10.1016/J.EST.2023.107227.

[3] S. Scaravonati, M. Sidoli, G. Magnani, A. Morenghi, M. Canova, J.H. Kim, M. Riccò, D. Pontiroli, Combined capacitive and electrochemical charge storage mechanism in high-performance graphene-based lithium-ion batteries, Mater. Today Energy 24 (2022) 100928, https://doi.org/10.1016/J.MTENER.2021.100928.

[4] L. Fornasini, S. Scaravonati, G. Magnani, A. Morenghi, M. Sidoli, D. Bersani, G. Bertoni, L. Aversa, R. Verucchi, M. Riccò, P.P. Lottici, D. Pontiroli, In situ decoration of laser-scribed graphene with TiO2 nanoparticles for scalable high-performance micro-supercapacitors, Carbon N Y 176 (2021) 296–306, https://doi.org/10.1016/J.CARBON.2021.01.129.

[5] B.K. Kim, S. Sy, A. Yu, J. Zhang, Electrochemical supercapacitors for energy storage and conversion, Handbook of Clean Energy Systems (2015) 1–25, https://doi.org/10.1002/9781118991978.HCES112.

[6] M. Sevilla, R. Mokaya, Energy storage applications of activated carbons: supercapacitors and hydrogen storage, Energy Environ. Sci. 7 (2014) 1250–1280, https://doi.org/10.1039/C3EE43525C.

[7] Y. Lv, J. Wang, D. Ji, J. Li, S. Zhao, Y. Zhao, Z. Cai, X. He, X. Sun, Carbonaceous electrode materials for supercapacitor: preparation and surface functionalization, Front. Energy Res. 10 (2023) 957032, https://doi.org/10.3389/FENRG.2022.957032/BIBTEX.

[8] Y. Qin, S. Jha, C. Hu, Z. Song, L. Miao, Y. Chen, P. Liu, Y. Lv, L. Gan, M. Liu, Hydrogen-bonded micelle assembly directed conjugated microporous polymers for nanospherical carbon frameworks towards dual-ion capacitors, J. Colloid Interface Sci. 675 (2024) 1091–1099, https://doi.org/10.1016/J.JCIS.2024.07.052.

[9] P. Liu, Z. Song, L. Miao, Y. Lv, L. Gan, M. Liu, Boosting spatial charge storage in ion-compatible pores of carbon superstructures for advanced zinc-ion capacitors, Small (2024) 2400774, https://doi.org/10.1002/SMLL.202400774.

[10] Y. Wang, L. Hao, Y. Zeng, X. Cao, H. Huang, J. Liu, X. Chen, S. Wei, L. Gan, P. Yang, M. Liu, D. Zhu, Three-dimensional hierarchical porous carbon derived from resorcinol formaldehyde-zinc tatrate/poly(styrene-maleic anhydride) for high performance supercapacitor electrode, J. Alloys Compd. 886 (2021) 161176, https://doi.org/10.1016/J.JALLCOM.2021.161176.

[11] Y. Wang, Y. Zeng, J. Zhu, C. Yang, H. Huang, X. Chen, R. Wang, P. Yan, S. Wei, M. Liu, D. Zhu, From dual-aerogels with semi-interpenetrating polymer network structure to hierarchical porous carbons for advanced supercapacitor electrodes,

Colloids Surf. A Physicochem. Eng. Asp. 649 (2022) 129356, https://doi.org/10.1016/J.COLSURFA.2022.129356.
[12] S. Sundriyal, V. Shrivastav, H.D. Pham, S. Mishra, A. Deep, D.P. Dubal, Advances in bio-waste derived activated carbon for supercapacitors: trends, challenges and prospective, Resour. Conserv. Recycl. 169 (2021) 105548, https://doi.org/10.1016/J.RESCONREC.2021.105548.
[13] D. Pontiroli, S. Scaravonati, G. Magnani, L. Fornasini, D. Bersani, G. Bertoni, C. Milanese, A. Girella, F. Ridi, R. Verucchi, L. Mantovani, A. Malcevschi, M. Riccò, Super-activated biochar from poultry litter for high-performance supercapacitors, Microporous Mesoporous Mater. 285 (2019) 161–169, https://doi.org/10.1016/J.MICROMESO.2019.05.002.
[14] A. Jain, S.K. Tripathi, Fabrication and characterization of energy storing supercapacitor devices using coconut shell based activated charcoal electrode, Mater. Sci. Eng., B 183 (2014) 54–60, https://doi.org/10.1016/J.MSEB.2013.12.004.
[15] H. Zhou, T. Fan, D. Zhang, Biotemplated materials for sustainable energy and environment: current status and challenges, ChemSusChem 4 (2011) 1344–1387, https://doi.org/10.1002/CSSC.201100048.
[16] A. Demirbaş, Biomass resource facilities and biomass conversion processing for fuels and chemicals, Energy Convers. Manag. 42 (2001) 1357–1378, https://doi.org/10.1016/S0196-8904(00)00137-0.
[17] N. Ahmad, A. Rinaldi, M. Sidoli, G. Magnani, A. Morenghi, S. Scaravonati, V. Vezzoni, L. Pasetti, L. Fornasini, F. Ridi, C. Milanese, M. Riccò, D. Pontiroli, High performance quasi-solid-state supercapacitor based on activated carbon derived from asparagus waste, J. Energy Storage 99 (2024) 113267, https://doi.org/10.1016/J.EST.2024.113267.
[18] P.N. Bhandari, A. Kumar, D.D. Bellmer, R.L. Huhnke, Synthesis and evaluation of biochar-derived catalysts for removal of toluene (model tar) from biomass-generated producer gas, Renew. Energy 66 (2014) 346–353, https://doi.org/10.1016/J.RENENE.2013.12.017.
[19] V. Kumar Vishwakarma, J. Kumar Gupta, P. Kumar Upadhyay, Pharmacological importance of Cucumis melo L.: an overview, Article Asian J. Pharmaceu. Clini. Res. 10 (2017), https://doi.org/10.22159/ajpcr.2017.v10i3.13849.
[20] R. Gómez-García, D.A. Campos, A. Oliveira, C.N. Aguilar, A.R. Madureira, M. Pintado, A chemical valorisation of melon peels towards functional food ingredients: bioactives profile and antioxidant properties, Food Chem. 335 (2021) 127579, https://doi.org/10.1016/J.FOODCHEM.2020.127579.
[21] P.M. Rolim, L.M.J. Seabra, G.R. de Macedo, Melon by-products: biopotential in human health and food processing, Food Rev. Int. 36 (2020) 15–38, https://doi.org/10.1080/87559129.2019.1613662.
[22] A.M.P. Marchetto, H.H. Ataide, M.L.F. Masson, Evaluation of wasted parts of food in the vegetable sector aiming its reuse, Demetra 9 (2008) 823–831.
[23] F. Caturla, M. Molina-Sabio, F. Rodríguez-Reinoso, Preparation of activated carbon by chemical activation with ZnCl2, Carbon N Y 29 (1991) 999–1007, https://doi.org/10.1016/0008-6223(91)90179-M.
[24] J. Pallarés, A. González-Cencerrado, I. Arauzo, Production and characterization of activated carbon from barley straw by physical activation with carbon dioxide and steam, Biomass Bioenergy 115 (2018) 64–73, https://doi.org/10.1016/J.BIOMBIOE.2018.04.015.
[25] A. Gundogdu, C. Duran, H.B. Senturk, M. Soylak, M. Imamoglu, Y. Onal, Physicochemical characteristics of a novel activated carbon produced from tea industry waste, J. Anal. Appl. Pyrolysis 104 (2013) 249–259, https://doi.org/10.1016/J.JAAP.2013.07.008.
[26] B. Seredyńska-Sobecka, M. Tomaszewska, M. Janus, A.W. Morawski, Biological activation of carbon filters, Water Res. 40 (2006) 355–363, https://doi.org/10.1016/J.WATRES.2005.11.014.
[27] S.Y. Jeong, J.W. Lee, Hydrothermal treatment, pretreatment of biomass: processes and technologies, 61–74, https://doi.org/10.1016/B978-0-12-800080-9.00005-0, 2015.
[28] A. Jain, R. Balasubramanian, M.P. Srinivasan, Hydrothermal conversion of biomass waste to activated carbon with high porosity: a review, Chem. Eng. J. 283 (2016) 789–805, https://doi.org/10.1016/J.CEJ.2015.08.014.
[29] N. Yadav Mohit, S.A. Hashmi, High energy density solid-state supercapacitors based on porous carbon electrodes derived from pre-treated bio-waste precursor sugarcane bagasse, J. Energy Storage 55 (2022) 105421, https://doi.org/10.1016/J.EST.2022.105421.
[30] N. Yadav, M.K. Singh, N. Yadav, S.A. Hashmi, High performance quasi-solid-state supercapacitors with peanut-shell-derived porous carbon, J. Power Sources 402 (2018) 133–146, https://doi.org/10.1016/J.JPOWSOUR.2018.09.032.
[31] F. Hu, A. Ragauskas, Pretreatment and lignocellulosic chemistry, Bioenergy Res 5 (2012) 1043–1066, https://doi.org/10.1007/S12155-012-9208-0/TABLES/15.
[32] X. Si, F. Lu, J. Chen, R. Lu, Q. Huang, H. Jiang, E. Taarning, J. Xu, A strategy for generating high-quality cellulose and lignin simultaneously from woody biomass, Green Chem. 19 (2017) 4849–4857, https://doi.org/10.1039/C7GC02492D.
[33] X. Yang, F. Zhang, L. Zhang, T. Zhang, Y. Huang, Y. Chen, A high-performance graphene oxide-doped ion gel as gel polymer electrolyte for all-solid-state supercapacitor applications, Adv. Funct. Mater. 23 (2013) 3353–3360, https://doi.org/10.1002/ADFM.201203556.
[34] W. Ren, C. Ding, X. Fu, Y. Huang, Advanced gel polymer electrolytes for safe and durable lithium metal batteries: challenges, strategies, and perspectives, Energy Storage Mater. 34 (2021) 515–535, https://doi.org/10.1016/J.ENSM.2020.10.018.
[35] J.P. Tafur, F. Santos, A.J. Fernández Romero, Influence of the ionic liquid type on the gel polymer electrolytes properties, Membranes 5 (2015) 752–771, https://doi.org/10.3390/MEMBRANES5040752, 5 (2015) 752–771.
[36] A. Gupta, A. Jain, S.K. Tripathi, Structural, Electrical and Electrochemical Studies of Ionic Liquid-Based Polymer Gel Electrolyte Using Magnesium Salt for Supercapacitor Application, vol. 28, 2021, p. 235, https://doi.org/10.1007/s10965-021-02597-9.
[37] M.Y. Bhat, N. Yadav, S.A. Hashmi, A high performance flexible gel polymer electrolyte incorporated with suberonitrile as additive for quasi-solid carbon supercapacitor, Mater. Sci. Eng., B 262 (2020) 114721, https://doi.org/10.1016/J.MSEB.2020.114721.
[38] J. Wang, G. Chen, S. Song, Na-ion conducting gel polymer membrane for flexible supercapacitor application, Electrochim. Acta 330 (2020) 135322, https://doi.org/10.1016/J.ELECTACTA.2019.135322.
[39] L. Wei, M. Sevilla, A.B. Fuertes, R. Mokaya, G. Yushin, Hydrothermal carbonization of abundant renewable natural organic chemicals for high-performance supercapacitor electrodes, Adv. Energy Mater. 1 (2011) 356–361, https://doi.org/10.1002/AENM.201100019.
[40] P. Kumari, S. Parveen, S.A. Hashmi, Diglyme-based “solvate ionic liquid” gelled in poly(vinylidine fluoride-co-hexafluoropropylene): a flexible electrolyte for high-performance magnesium-ion batteries, ACS Appl. Energy Mater. 6 (2023) 12468–12481, https://doi.org/10.1021/ACSAEM.3C02404/ASSET/IMAGES/LARGE/AE3C02404_0008.JPEG.
[41] N. Yadav, S.A. Hashmi, Energy enhancement of quasi-solid-state supercapacitors based on a non-aqueous gel polymer electrolyte via a synergistic effect of dual redox additives diphenylamine and potassium iodide, J Mater Chem A Mater 8 (2020) 18266–18279, https://doi.org/10.1039/D0TA06331B.
[42] A.A. Hor, S.A. Hashmi, Optimization of hierarchical porous carbon derived from a biomass pollen-cone as high-performance electrodes for supercapacitors, Electrochim. Acta 356 (2020) 136826, https://doi.org/10.1016/J.ELECTACTA.2020.136826.
[43] Z. Hei, S. Wu, H. Zheng, H. Liu, H. Duan, Increasing the electrochemical stability window for polyethylene-oxide-based solid polymer electrolytes by understanding the affecting factors, Solid State Ionics 375 (2022) 115837, https://doi.org/10.1016/J.SSI.2021.115837.
[44] B. Liu, Y. Huang, H. Cao, L. Zhao, Y. Huang, A. Song, Y. Lin, X. Li, M. Wang, A novel porous gel polymer electrolyte based on poly(acrylonitrile-polyhedral oligomeric silsesquioxane) with high performances for lithium-ion batteries, J. Membr. Sci. 545 (2018) 140–149, https://doi.org/10.1016/J.MEMSCI.2017.09.077.
[45] Y. Wang, L. Fu, L. Shi, Z. Wang, J. Zhu, Y. Zhao, S. Yuan, Gel polymer electrolyte with high Li + transference number enhancing the cycling stability of lithium anodes, ACS Appl. Mater. Interfaces 11 (2019) 5168–5175, https://doi.org/10.1021/ACSAMI.8B21352/ASSET/IMAGES/LARGE/AM-2018-21352Q_0009.JPEG.
[46] S. Zugmann, M. Fleischmann, M. Amereller, R.M. Gschwind, H.D. Wiemhöfer, H.J. Gores, Measurement of transference numbers for lithium ion electrolytes via four different methods, a comparative study, Electrochim. Acta 56 (2011) 3926–3933, https://doi.org/10.1016/J.ELECTACTA.2011.02.025.
[47] C. Bläker, J. Muthmann, C. Pasel, D. Bathen, Characterization of activated carbon adsorbents – state of the art and novel approaches, ChemBioEng Rev. 6 (2019) 119–138, https://doi.org/10.1002/CBEN.201900008.
[48] C. Martín, P. Dixit, F. Momayez, L.J. Jönsson, Hydrothermal pretreatment of lignocellulosic feedstocks to facilitate biochemical conversion, Front. Bioeng. Biotechnol. 10 (2022) 846592, https://doi.org/10.3389/FBIOE.2022.846592/BIBTEX.
[49] F. Tuinstra, J.L. Koenig, Raman spectrum of graphite, J. Chem. Phys. 53 (1970) 1126–1130, https://doi.org/10.1063/1.1674108.
[50] A. Ferrari, J. Robertson, Interpretation of Raman spectra of disordered and amorphous carbon, Phys. Rev. B 61 (2000) 14095–14107, https://doi.org/10.1103/PHYSREVB.61.14095.
[51] L.G. Cançado, M.A. Pimenta, B.R.A. Neves, M.S.S. Dantas, A. Jorio, Influence of the atomic structure on the Raman spectra of graphite edges, Phys. Rev. Lett. 93 (2004) 247401, https://doi.org/10.1103/PHYSREVLETT.93.247401/FIGURES/4/MEDIUM.
[52] L.M. Malard, M.A. Pimenta, G. Dresselhaus, M.S. Dresselhaus, Raman spectroscopy in graphene, Phys. Rep. 473 (2009) 51–87, https://doi.org/10.1016/J.PHYSREP.2009.02.003.
[53] N. Yadav, Promila Ritu, S.A. Hashmi, Hierarchical porous carbon derived from eucalyptus-bark as a sustainable electrode for high-performance solid-state supercapacitors, Sustain. Energy Fuels 4 (2020) 1730–1746, https://doi.org/10.1039/C9SE00812H.
[54] N. Yadav, N. Yadav, S.A. Hashmi, Ionic liquid incorporated, redox-active blend polymer electrolyte for high energy density quasi-solid-state carbon supercapacitor, J. Power Sources 451 (2020) 227771, https://doi.org/10.1016/J.JPOWSOUR.2020.227771.
[55] P.L. Taberna, P. Simon, J.F. Fauvarque, Electrochemical characteristics and impedance spectroscopy studies of carbon-carbon supercapacitors, J. Electrochem. Soc. 150 (2003) A292, https://doi.org/10.1149/1.1543948/XML.
[56] N. Yadav, N. Yadav, M.K. Singh, S.A. Hashmi, Nonaqueous, redox-active gel polymer electrolyte for high-performance supercapacitor, Energy Technol. 7 (2019) 1900132, https://doi.org/10.1002/ENTE.201900132.
[57] B. Akinwolemiwa, C. Peng, G.Z. Chen, Redox electrolytes in supercapacitors, J. Electrochem. Soc. 162 (2015) A5054–A5059, https://doi.org/10.1149/2.0111505JES/XML.
[58] T.S. Mathis, N. Kurra, X. Wang, D. Pinto, P. Simon, Y. Gogotsi, Energy storage data reporting in perspective—guidelines for interpreting the performance of electrochemical energy storage systems, Adv. Energy Mater. 9 (2019) 1902007, https://doi.org/10.1002/AENM.201902007.

[59] C. Qiu, L. Jiang, Y. Gao, L. Sheng, Effects of oxygen-containing functional groups on carbon materials in supercapacitors: a review, Mater. Des. 230 (2023) 111952, https://doi.org/10.1016/J.MATDES.2023.111952.

[60] S.A. Hashmi Mohit, Biodegradable poly-ε-caprolactone based porous polymer electrolytes for high performance supercapacitors with carbon electrodes, J. Power Sources 557 (2023) 232548, https://doi.org/10.1016/J.JPOWSOUR.2022.232548.

[61] S.A. Hashmi, M. Yasir Bhat, N. Yadav, Gel polymer electrolyte composition incorporating adiponitrile as a solvent for high-performance electrical double-layer capacitor, ACS Appl. Energy Mater. 3 (2020) 10642–10652, https://doi.org/10.1021/ACSAEM.0C01690/ASSET/IMAGES/LARGE/AE0C01690_0008.JPEG.

[62] L. Huang, Q. Wu, S. Liu, S. Yu, A.J. Ragauskas, Solvent-free production of carbon materials with developed pore structure from biomass for high-performance supercapacitors, Ind. Crops Prod. 150 (2020) 112384, https://doi.org/10.1016/J.INDCROP.2020.112384.

[63] B. Jia, Q. Mian, D. Wu, T. Wang, Heteroatoms self-doped porous carbon from cottonseed meal using K2CO3 as activator and DES electrolyte for supercapacitor with high energy density, Mater. Today Chem. 24 (2022), https://doi.org/10.1016/J.MTCHEM.2022.100828.

[64] D.A. Khuong, T.T. Kieu, Y. Nakaoka, T. Tsubota, D. Tashima, H.N. Nguyen, D. Tanaka, The investigation of activated carbon by K2CO3 activation: micropores- and macropores-dominated structure, Chemosphere 299 (2022), https://doi.org/10.1016/J.CHEMOSPHERE.2022.134365.

[65] E. Taer, D. Afdal Yusra, A. Amri, Awitdrus, R. Taslim, Agustino Apriwandi, A. Putri, The synthesis of activated carbon made from banana stem fibers as the supercapacitor electrodes, Mater. Today Proc. 44 (2020) 3346–3349, https://doi.org/10.1016/J.MATPR.2020.11.645.

[66] Z. Xiao, W. Chen, K. Liu, P. Cui, D. Zhan, ELECTROCHEMICAL SCIENCE porous biomass carbon derived from peanut shells as electrode materials with enhanced electrochemical performance for supercapacitors, Int. J. Electrochem. Sci. 13 (2018) 5370–5381, https://doi.org/10.20964/2018.06.54.

[67] M.Y. Bhat, N. Yadav, S.A. Hashmi, Pinecone-derived porous activated carbon for high performance all-solid-state electrical double layer capacitors fabricated with flexible gel polymer electrolytes, Electrochim. Acta 304 (2019) 94–108, https://doi.org/10.1016/J.ELECTACTA.2019.02.092.

[68] K. Charoensook, C.L. Huang, H.C. Tai, V.V.K. Lanjapalli, L.M. Chiang, S. Hosseini, Y.T. Lin, Y.Y. Li, Preparation of porous nitrogen-doped activated carbon derived from rice straw for high-performance supercapacitor application, J. Taiwan Inst. Chem. Eng. 120 (2021) 246–256, https://doi.org/10.1016/j.jtice.2021.02.021.

[69] Z. Huang, C. Qin, J. Wang, L. Cao, Z. Ma, Q. Yuan, Z. Lin, P. Zhang, Research on high-value utilization of carbon derived from tobacco waste in supercapacitors, Materials 14 (2021) 1714, https://doi.org/10.3390/MA14071714, 1714 14 (2021).

[70] W.H. Qu, Y.Y. Xu, A.H. Lu, X.Q. Zhang, W.C. Li, Converting biowaste corncob residue into high value added porous carbon for supercapacitor electrodes, Bioresour. Technol. 189 (2015) 285–291, https://doi.org/10.1016/J.BIORTECH.2015.04.005.

[71] C. Huang, T. Sun, D. Hulicova-Jurcakova, Wide electrochemical window of supercapacitors from coffee bean-derived phosphorus-rich carbons, ChemSusChem 6 (2013) 2330–2339, https://doi.org/10.1002/CSSC.201300457.

[72] M. Chen, X. Kang, T. Wumaier, J. Dou, B. Gao, Y. Han, G. Xu, Z. Liu, L. Zhang, Preparation of activated carbon from cotton stalk and its application in supercapacitor, J. Solid State Electrochem. 17 (2013) 1005–1012, https://doi.org/10.1007/S10008-012-1946-6.

[73] R.H.I. Keyla, G.T.L. Leticia, S.C.E. Maximiano, T.G.L. Carlos, Activated carbon from agave wastes (agave tequilana) for supercapacitors via potentiostatic floating test, J. Mater. Sci. Mater. Electron. 32 (2021) 21432–21440, https://doi.org/10.1007/S10854-021-06649-0/FIGURES/8.